A method for evaluating bias in global measurements of CO_2 total columns from space

D. Wunch[1], P. O. Wennberg[1], G. C. Toon[1,2], B. J. Connor[3], B. Fisher[2], G. B. Osterman[2], C. Frankenberg[2], L. Mandrake[2], C. O'Dell[4], P. Ahonen[5], S. C. Biraud[14], R. Castano[2], N. Cressie[6], D. Crisp[2], N. M. Deutscher[7,8], A. Eldering[2], M. L. Fisher[14], D. W. T. Griffith[8], M. Gunson[2], P. Heikkinen[5], G. Keppel-Aleks[1], E. Kyrö[5], R. Lindenmaier[15], R. Macatangay[8], J. Mendonca[15], J. Messerschmidt[7], C. E. Miller[2], I. Morino[9], J. Notholt[7], F. A. Oyafuso[2], M. Rettinger[10], J. Robinson[12], C. M. Roehl[1], R. J. Salawitch[11], V. Sherlock[12], K. Strong[15], R. Sussmann[10], T. Tanaka[9,*], D. R. Thompson[2], O. Uchino[9], T. Warneke[7], and S. C. Wofsy[13]

[1]California Institute of Technology, Pasadena, CA, USA
[2]Jet Propulsion Laboratory, California Institute of Technology, Pasadena, CA, USA
[3]BC Consulting, Ltd., Alexandra, New Zealand
[4]Colorado State University, Fort Collins, CO, USA
[5]Arctic Research Centre of the Finnish Meteorological Institute, Helsinki, Finland
[6]Department of Statistics, The Ohio State University, Columbus, OH, USA
[7]University of Bremen, Bremen, Germany
[8]University of Wollongong, Wollongong, NSW, Australia
[9]National Institute for Environmental Studies, Tsukuba, Japan
[10]IMK-IFU, Garmisch-Partenkirchen, Germany
[11]Atmospheric & Oceanic Science, University of Maryland, College Park, MD, USA
[12]National Institute of Water & Atmospheric Research, Wellington, New Zealand
[13]Harvard University, Cambridge, MA, USA
[14]Lawrence Berkeley National Laboratories, Berkeley, CA, USA**
[15]Department of Physics, University of Toronto, Toronto, ON, Canada
[*]now at: Japan Aerospace Exploration Agency, Tsukuba, Japan

Correspondence to: D. Wunch (dwunch@gps.caltech.edu)

**Biraud is partially supported by the US. Department of Energy under Contract No. DE-AC02-05CH11231.

Abstract. We describe a method of evaluating systematic errors in measurements of total column dry-air mole fractions of CO_2 (X_{CO_2}) from space, and we illustrate the method by applying it to the Atmospheric CO_2 Observations from Space retrievals of the Greenhouse Gases Observing Satellite (ACOS-GOSAT) v2.8. The approach exploits the lack of large gradients in X_{CO_2} south of 25° S to identify large-scale offsets and other biases in the ACOS-GOSAT data with several retrieval parameters and errors in instrument calibration. We demonstrate the effectiveness of the method by comparing the ACOS-GOSAT data in the Northern Hemisphere with ground truth provided by the Total Carbon Column Observing Network (TCCON). We use the correlation between free-tropospheric temperature and X_{CO_2} in the Northern Hemisphere to define a dynamically informed coincidence criterion between the ground-based TCCON measurements and the ACOS-GOSAT measurements. We illustrate that this approach provides larger sample sizes, hence giving a more robust comparison than one that simply uses time, latitude and longitude criteria. Our results show that the agreement with the TCCON data improves after accounting for the systematic errors. A preliminary evaluation of the improved v2.9 ACOS-GOSAT data is also discussed.

1 Introduction

The Greenhouse Gases Observing Satellite (GOSAT) was successfully launched on 23 January 2009, with the goal of measuring total column abundances of CO_2 and CH_4 with unprecedented precision from space (Yokota et al., 2004). GOSAT is a joint venture of the National Institute for Environmental Studies (NIES), the Japanese Space Agency (JAXA) and the Ministry of the Environment (MOE), and carries the Thermal And Near-infrared Sensor for carbon Observation Fourier Transform Spectrometer (TANSO-FTS, Hamazaki et al., 2005), which measures spectra of sunlight reflected from the Earth. Preliminary validation of the NIES/JAXA/MOE GOSAT products is reported in Morino et al. (2011). Two independent retrieval algorithms are presented and validated in Butz et al. (2011) for CO_2 and CH_4 and in Parker et al. (2011) for CH_4.

The Atmospheric CO_2 Observations from Space (ACOS) project was formed from the Orbiting Carbon Observatory (OCO) project following the OCO launch failure in February 2009. Under an agreement with NIES, JAXA, and the MOE, the ACOS team applied the OCO retrieval algorithm to the GOSAT spectra to compute column-averaged dry-air mole fractions of CO_2 (denoted X_{CO_2}). In this paper, we discuss the evaluation of the ACOS-GOSAT X_{CO_2} data product by comparing it with more precise and accurate X_{CO_2} measurements from the ground-based Total Carbon Column Observing Network (TCCON, Wunch et al., 2011). The TCCON measurements are calibrated to World Meteorological Organization (WMO) standards through comparisons with integrated aircraft profiles (Washenfelder et al., 2006; Deutscher et al., 2010; Wunch et al., 2010; Messerschmidt et al., 2011), and have a precision and accuracy of $\sim$0.8 ppm (2σ, Wunch et al., 2010). The locations of the stations used in this study are shown in Fig. 1.

Our technical approach for evaluating the X_{CO_2} product from the ACOS-GOSAT retrievals makes use of the relatively spatially uniform CO_2 in the Southern Hemisphere to identify systematic errors, including large-scale biases and other artifacts caused by the retrieval algorithm or errors in the instrument calibration. Once identified, these biases are removed and the success of this modification to the data is evaluated through comparisons with the Northern Hemisphere TCCON data. We exploit observed correlations between free-troposphere potential temperature and X_{CO_2} to minimize variability in X_{CO_2} that is dynamic in origin (Keppel-Aleks et al., 2011) when defining coincidence criteria in the Northern Hemisphere. This better defines comparable observations than using a simple geographic constraint.

In Sect. 2, we detail our approach to comparing global X_{CO_2} measurements against the TCCON X_{CO_2} measurements. We then describe the ACOS-GOSAT X_{CO_2} data product and screening procedures in Sect. 3. The techniques are applied and evaluated in Sect. 4 and Sect. 5, and a discussion and conclusions follow in Sect. 6.

2 Comparing satellite-based X_{CO_2} with ground-based TCCON measurements

Observations and models of surface, partial and total column amounts of CO_2 in the Southern Hemisphere show low seasonal and geographic variability compared with the Northern Hemisphere. Observations from the global network of in situ atmospheric CO_2 measurements show that surface CO_2 concentrations at latitudes between 25° S and 55° S have a small seasonal cycle ($\sim$1 ppm peak-to-peak), and small geographic gradients (GLOBALVIEW-CO_2, 2006). Olsen and Randerson (2004) predicted such uniformity in modeling the total columns of CO_2 in the Southern Hemisphere. Measurements of CO_2 profiles from the recent Hiaper Pole-to-Pole Observations (HIPPO) campaign by Wofsy et al. (2011) also show that the Southern Hemisphere CO_2 field does not vary by more than 1.6 ppm south of 25° S. Figure 2 shows the HIPPO CO_2 data centred on the Pacific Ocean.

There are two TCCON stations located south of 25° S: Wollongong, Australia (34° S) and Lauder, New Zealand (45° S). Wollongong is located on the Australian eastern coast, on the outskirts of a small urban centre, located about 100 km south of Sydney. Lauder is located on New Zealand's south island and predominantly samples clean maritime air. The Lauder site has a seasonal cycle in X_{CO_2} with a small peak-to-peak amplitude of about 0.6 ppm (Fig. 3). The measurements over Wollongong are affected by local pollutants which can increase the seasonal cycle of X_{CO_2} over Wollongong to $\sim$2 ppm peak-to-peak, but this is variable from year to year. When the effect from the pollution is accounted for, the background seasonal cycle is reduced to $\sim$1 ppm peak-to-peak. The Lauder X_{CO_2} time series is the longest in the Southern Hemisphere, and has a secular increase of 1.89 ppm yr^{-1} since 2004, which is in good agreement with the global mean secular increase of about 2 ppm yr^{-1} (with a year-to-year variability of 0.3 ppm yr^{-1}, 1σ) from the GLOBALVIEW surface in situ flask network over the same time period (Conway and Tans, 2011).

Consistent with HIPPO, TCCON, and GLOBALVIEW, we assume that the Southern Hemisphere poleward of 25° S has a small seasonal cycle in X_{CO_2} of ∼0.6 ppm (peak-to-peak), has no geographic gradients and a secular increase of 1.89 ppm yr^{-1}. We assume that measurements of X_{CO_2} in this region that show spatial and temporal variations that exceed this constraint contain spurious variance, and we look for empirical correlations of X_{CO_2} with retrieval or instrument parameters that explain the variance. We assume that these correlations represent systematic errors that exist globally. After accounting for these biases, the satellite X_{CO_2} data are compared against TCCON data globally. This procedure is applicable to any global measurement of X_{CO_2}, including the Scanning Imaging Absorption Spectrometer for Atmospheric Chartography (SCIAMACHY Burrows et al., 1995), GOSAT and the future OCO-2 and OCO-3 instruments. We will apply it to the ACOS-GOSAT X_{CO_2} in the following sections.

3 ACOS-GOSAT data product

The ACOS-GOSAT data processing algorithm is described in detail in O'Dell et al. (2011). It is adapted from the OCO retrieval algorithm (Boesch et al., 2006; Connor et al., 2008; Boesch et al., 2011) and incorporates modifications required to accurately represent the physics of the GOSAT instrument, such as the instrument line shape and noise model. The inverse method is based on the optimal estimation approach given by Rodgers (2000). The forward model is based on LIDORT (Spurr et al., 2001; Spurr, 2002), and a two-order scattering model to account for polarization, described by Natraj and Spurr (2007). A "low-streams interpolation" scheme, devised by O'Dell (2010), ensures that the scattering calculation is both fast and accurate.

The molecular absorption coefficients for CO_2 (Toth et al., 2008) and O_2 (Long et al., 2010) have been extended to account for line mixing and collision-induced absorption using the results of Hartmann et al. (2009) for CO_2 and of Tran and Hartmann (2008) for O_2. The disk-integrated solar spectrum is based on ground-based measurements from the Kitt Peak Fourier transform spectrometer. All other molecular spectral parameters are taken from HITRAN 2008 (Rothman et al., 2009). Surface pressure is retrieved from the oxygen A-band near 0.76 µm. The CO_2 columns are retrieved from the weak band near 1.61 µm, and the strong band near 2.1 µm. The spectral ranges used in the ACOS algorithm match those of the OCO and future OCO-2 instrument.

3.1 ACOS-GOSAT data screening

We use the v2.8 release of the ACOS-GOSAT data, available from the Goddard Data and Information Services Center (GDISC, see note ACOS-GOSAT Data Access), spanning 5 April 2009 through 21 March 2011. Using the method described in Taylor et al. (2011) and O'Dell et al. (2011), these retrievals are pre-screened to include only cloud-free scenes. The ACOS-GOSAT data product includes a "master quality flag" that provides an estimate of confidence in the retrieved X_{CO_2} and

its associated a posteriori error. The master quality flag uses filters that are described in the ACOS readme document also available from the GDISC (Savtchenko and Avis, 2010). Here, we apply post-processing filters that are slightly different from those used to derive the master quality flag provided with the data. The filters as applied are listed in Table 1 and are chosen to limit the retrievals to those in which we have the highest confidence. The main differences between the filters applied here and those used to determine the master quality flag are in the quality of the spectral fit (i.e., reduced χ^2), the allowed deviation of the retrieved surface pressure from the a priori, and a few additional filters as described below.

Retrievals are defined as successful by the master quality flag when they satisfy $\chi^2 < 1.2$. However, the χ^2 values have increased linearly over time, because the time-dependent radiometric calibration owing to a sensitivity degradation of the O_2 A-band channel was not applied to the noise model. To compensate for this, we adjust the cutoff value so that it starts at 1.2 and evolves with a linear increase in time, matching the increase in minimum χ^2. As a result, a similar number of scenes are retained over time.

Data with retrieved surface pressure (P_{surf}) that differs significantly from the ECMWF a priori surface pressure (P_{ECMWF}) are marked as 'bad' in the master quality flag. Data are retained by the master quality flag when the difference between the retrieved and a priori surface pressures:

$$\Delta P \equiv (P_{\mathrm{surf}} - P_{\mathrm{ECMWF}}) \tag{1}$$

is $0 < \Delta P < 20\,\mathrm{hPa}$. In this work, scenes are retained that satisfy: $|(\Delta P) - \overline{(\Delta P)}| < 5\,\mathrm{hPa}$. The global mean value of $\overline{\Delta P}$ is approximately $10.9\,\mathrm{hPa}$.

We apply three additional filters: one to remove the medium-gain scenes, one to remove the glint measurements, and one to remove scenes that contain surface ice or snow. The medium-gain (M-gain) TANSO-FTS mode, which is used over very bright surface scenes (Fig. 1), is known to have ghosting issues caused by mismatched timing delays in the signal chain (Suto and Kuze, 2010). In future releases of the spectra, this ghosting effect will be corrected, but in the meantime, we do not use the M-gain data. Glint measurements are made exclusively over ocean and have different properties than the nadir measurements made over land. The ACOS-GOSAT glint retrieval algorithm requires additional refinement, so glint retrievals are not considered here.

A fraction of the ACOS-GOSAT retrievals exhibit anomalous $\mathrm{X_{CO_2}}$ values due to the presence of the higher-albedo snow- and ice-covered land surfaces, which are indistinguishable from low-lying cloud or aerosol in the current version of the algorithm. We apply a filter that depends on the retrieved albedos of the O_2 A-band ($A_{\mathrm{AO_2}}$) and the strong CO_2 band ($A_{\mathrm{SCO_2}}$). We will call this combination of albedos the "blended albedo." The blended albedo was determined from a multivariate linear regression on the data, which was trained on scenes known to have snow or ice conditions at the surface, and correctly characterises over 99.9 % of the scenes. Data that are retained satisfy Eq. (2),

and their distribution is shown in Fig. 4

$$\text{blended albedo} \equiv 2.4 A_{\mathrm{AO_2}} - 1.13 A_{\mathrm{SCO_2}} < 1. \tag{2}$$

4 Bias determination from the Southern Hemisphere

The filtering described in Sect. 3.1 removes spectra recorded under atmospheric conditions that are not yet modeled well in the ACOS retrieval (e.g., surface ice). However, these filters do not remove all systematic errors in the treatment of the instrument calibration, spectroscopy, measurement geometry, or other features. This section discusses the identification of these biases.

Known deficiencies in the implementation of the spectroscopic line shape of the O_2 A-band and the strong CO_2 bands cause systematic biases in the retrieved X_{CO_2}. In the absence of an improved line shape model (currently under development), the biases can either be removed after the retrieval by calibrating against known X_{CO_2} values, or by scaling the cross-sections before the retrieval. The method that will be employed by the ACOS team in the 2.9 version of the algorithm (Appendix B) is to scale the cross-sections of the O_2 A-band in order to retrieve the known column of atmospheric O_2, and to ensure that the spectroscopic parameters describing the strong CO_2 band result in a retrieval that yields the same column amount as the weak CO_2 band for the same atmospheric conditions. The v2.8 algorithm does not use scaled cross-sections, so here we perform an initial "calibration" of the ACOS-GOSAT X_{CO_2} data using Southern Hemisphere TCCON data. The mean ratio between the summertime (December, January, February) Lauder TCCON data and the corresponding ACOS-GOSAT data within $\pm 5°$ latitude of Lauder is $\sim 2\,\%$. We have thus corrected this bias globally by dividing all ACOS-GOSAT data by 0.982 (Fig. 5). Much of this bias is due to the retrieved surface pressure offset (ΔP), described in Sect. 3.1.

From the v2.8 release of the ACOS-GOSAT product, we select the most significant parameters that reduce the variance of the X_{CO_2} anomalies in the Southern Hemisphere south of 25° S. The anomalies are computed by subtracting a $1.89\,\mathrm{ppm\,yr^{-1}}$ slope with a seasonal cycle derived from the Baring Head, New Zealand GLOBALVIEW seasonal climatology (GLOBALVIEW-CO_2, 2006) from the ACOS-GOSAT data between 25° S and 55° S. Because the GLOBALVIEW data replicate the in situ seasonal cycle at the surface and not the column seasonal cycle, we have applied a time lag of 6 weeks and have reduced the amplitude by multiplying by 0.65 to best match the seasonal cycles at Lauder and Wollongong (Fig. 3).

In order of importance, the most significant parameters correlated with this spurious variability in the retrieved X_{CO_2} are the blended albedo (defined in Eq. 2), ΔP (defined in Eq. 1), airmass (described in Eq. 3 below), and the continuum level of the O_2 A-band spectral radiance (called "signal_o2" in the v2.8 data files). The airmass is approximated by

$$\text{airmass} = 1/\cos(\text{solar zenith angle}) + 1/\cos(\text{observing angle}), \tag{3}$$

where solar zenith angle is the angle of the sun, and observing angle is the off-nadir viewing angle of the instrument. (These parameters are labeled "sounding_solar_zenith," and "sounding_zenith," respectively, in the v2.8 data files.)

A multivariate linear regression on the blended albedo, ΔP (in hPa), the airmass, and the signal_o2 (in W cm^{-2} sr^{-1} (cm^{-1})$^{-1}$) suggests that the following modification to the retrieved X_{CO_2} (in ppm) partially removes the biases:

$$\begin{aligned} X_{CO_2}^{\text{modified}} = & \frac{X_{CO_2}^{\text{retrieved}}}{C_0} - C_1(\text{blended_albedo} - \overline{\text{blended_albedo}}) - C_2(\Delta P - \overline{\Delta P}) \\ & - C_3(\text{airmass} - \overline{\text{airmass}}) - C_4\left(\text{signal_o2} \times 10^7 - \overline{\text{signal_o2}} \times 10^7\right) \end{aligned} \quad (4)$$

where the coefficients are $C_0 = 0.982$, $C_1 = 10.5$ ppm/units of blended albedo, $C_2 = -0.15$ ppm hPa^{-1}, $C_3 = -2.0$ ppm/airmass and $C_4 = -0.25$ ppm/ (10^7W cm^{-2} sr^{-1} (cm^{-1})$^{-1}$). Subtracting off the mean values, listed in Table 2, minimizes the overall change in X_{CO_2}. Scatter plots of the simultaneous regressions are shown in Fig. 6. If only the secular increase is removed from the Southern Hemisphere data to produce the anomalies (i.e., if we do not include the small seasonal cycle), the regression coefficients agree within two bootstrapped standard errors with the coefficients in Eq. (4). Further, if we apply a -1 ppm gradient between 25° S and 55° S to approximate the HIPPO observations, the coefficients again agree, within two bootstrapped standard errors (see Table 2). The bootstrapping technique is described by, for example, Efron and Gong (1983).

These basis functions (blended albedo, ΔP, airmass, signal_o2) are not orthogonal, and other parameters may be used to accomplish a similar reduction in the variability of retrieved X_{CO_2}. Errors in aerosol and cloud characterization or identification can affect the retrieved albedos and hence the blended albedo parameter, and they can also affect the retrieved path length and ΔP. However, blended albedo and ΔP are known to have spurious relationships with X_{CO_2} in simulated data (O'Dell et al., 2011) from an orbit simulator developed by O'Brien et al. (2009) as a test bed for the OCO algorithm. The simulator contains no errors due to spectroscopy or the instrument, and hence provides a direct test of the retrieval algorithm. (It is worth noting that O'Dell et al. (2011) do not use the blended albedo parameter directly, but they use the ratio of the weak CO_2 band signal to the O_2 A-band signal, which is strongly and linearly related to blended albedo (r^2=0.78).) This suggests that at least part of the blended albedo-X_{CO_2} and ΔP-X_{CO_2} relationships are caused by the retrieval algorithm itself.

In addition to parameters that can be tested in the simulator, there are several known causes of systematic effects on the retrievals. First, errors in the spectroscopy can produce spurious airmass dependencies as well as global biases (e.g., Yang et al., 2005; Hartmann et al., 2009; Deutscher et al., 2010; Wunch et al., 2011) and can affect the pressure retrieval (e.g., ΔP). Another error source is from nonlinearities in the instrument signal chain that can manifest themselves as zero-level offsets in the O_2 A-band. Zero-level offsets in a Fourier transform spectrometer depend strongly on the

signal at zero path difference, and hence on the average signal level of the spectrum (Abrams et al., 1994). As a proxy for the average signal level, which is not available in the public v2.8 data, we use the continuum level radiance ("signal_o2"), which is highly correlated with the average signal level ($r^2 = 0.994$). Disentangling biases associated with the spectral continuum level from the airmass is difficult, because they are strongly (and nonlinearly) anti-correlated.

Future releases of data will account for the zero-level offset explicitly, either as in Butz et al. (2011), or, preferably, in the measured radiances in the interferograms, prior to the Fourier transform, once the underlying instrumental cause is properly quantified.

Finally, there is a photosynthetic fluorescence signal in the O_2 A-band (Frankenberg et al., 2011; Joiner et al., 2011). Its potential impact on the retrieval of scattering properties in the A-band is described by Frankenberg et al. (2011) and makes use of the Fraunhofer lines near the O_2 A-band. This effect is currently ignored in the X_{CO_2} retrievals and can give rise to systematic biases. Over photosynthetically active regions of the globe, the vegetation fluoresces, adding a broad-band signal throughout the O_2 A-band. If this additional signal is not included in the forward model, the measured O_2 lines appear shallower than expected, and the retrieved X_{CO_2} will be incorrect (too high), with a seasonal cycle from the vegetation fluorescence imposed on top of the true X_{CO_2} seasonal cycle that is of interest here. The effects of fluorescence will be retrieved and the fluorescence data will be available in a future release of the ACOS-GOSAT data.

In applying Eq. (4) to the global dataset, we assume that the dependencies of ΔX_{CO_2} on the parameters are linear, and can be reasonably extrapolated to values found outside the range in the Southern Hemisphere. The Northern Hemisphere and Southern Hemisphere have similar distributions of ΔP, blended albedo and signal_o2, but the Northern Hemisphere data contain a larger range of airmasses. In the Southern Hemisphere, 99 % of the data poleward of 25° S have sampled airmasses between 2 and 3.3. In the Northern Hemisphere, 99 % of the data poleward of 25° N have sampled airmasses between 2 and 5.1. Any nonlinearity in the airmass-ΔX_{CO_2} relationship will result in a residual airmass dependency in the modified Northern Hemisphere data. Maps and histograms of the four parameters are in the supplementary material (Figs. S1 and S2).

4.1 Applying averaging kernels

To compare two X_{CO_2} observations properly, the retrievals must be computed about a common a priori profile, and the effect of smoothing must be taken into account by applying the averaging kernels (Rodgers and Connor, 2003). Since the v2.8 ACOS and TCCON retrievals were computed using different a priori profiles, we must adjust the retrieved X_{CO_2} values accordingly (see Sect. A for the mathematical details). To test the effect of this adjustment and of the smoothing, we select retrievals within $\pm 0.5°$ latitude and $\pm 1°$ longitude of the Lamont TCCON site. We cannot test the effects of the averaging kernels globally because this requires an estimate of the real atmospheric variability everywhere, which is unknown. We can generate an estimate of the atmospheric vari-

ability over Lamont, however, by using the bi-weekly low-altitude (0–5 km) aircraft measurements of CO_2 profiles over the Lamont TCCON station (Fig. 7) and the surface CO_2 measurements from the co-located tall tower when they were available. Each profile was extrapolated up to 5500 m and down to the surface altitude (315 m) from the nearest available data point, resulting in 177 profiles recorded between January 2006 and November 2009. In order to compute the weekly variance over several years of observations, a secular increase of 1.89 ppm yr^{-1} was subtracted from all altitudes of the profiles. Next, we adjust the ACOS-GOSAT values to the ensemble profile, which we assume to be the TCCON a priori profile. This results in an adjustment to the ACOS-GOSAT X_{CO_2} that is seasonal, with an amplitude of about 0.5 ppm. It may also have a small secular decrease of about 0.1 ppm yr^{-1} as well, which could be due to the differences in the secular increases in the ACOS-GOSAT and TCCON a priori profiles. The ACOS X_{CO_2} values are adjusted downward in the winter, and upward in the summer, which has the effect of reducing the overall seasonal cycle of the ACOS-GOSAT retrieval (Fig. 8). The adjustment at Lamont has a seasonal cycle because the ACOS-GOSAT a priori profile does not contain a seasonal cycle, whereas the real atmosphere does (Fig. A1). This seasonal cycle is driven near the surface by biospheric respiration and uptake, and in the stratosphere by dynamics that seasonally alter the tropopause height. The adjustment to the ACOS-GOSAT data will be latitude-dependent, with smaller adjustments in the Southern Hemisphere, and the largest adjustments at the latitude of the Boreal forests (i.e., around 50–65° N), where the surface seasonal cycle has the largest amplitude. Figure S3 illustrates the latitude-dependence of the adjustment.

The smoothing error (defined in the caption and given by the red curve in Fig. 8) is about 0.6 ppm, which is smaller than the sum of the variances of the ACOS-GOSAT X_{CO_2} and the TCCON X_{CO_2} ($\sim$1.5 ppm) but not negligibly so. The effect of smoothing the TCCON data using the ACOS-GOSAT averaging kernel results in a bias of about 0.6 ppm with no significant seasonal cycle or airmass dependence (the yellow curve in Fig. 8).

Applying the averaging kernels in a globally consistent manner is not possible without a global estimate of atmospheric variability. However, we can draw two important conclusions from the Lamont test:

1. There is a seasonal cycle induced by the adjustment of the ACOS-GOSAT data to the TCCON a priori profile. The amplitude of the adjustment has a latitude dependence and is about 0.5 ppm at Lamont.

2. There is a bias of about 0.6 ppm induced by smoothing the TCCON profile with the ACOS-GOSAT averaging kernel at Lamont.

The TCCON a priori profile is being evaluated for a future version of the ACOS-GOSAT algorithm, which would make the adjustment step unnecessary.

Our correction scheme described by Eq. (4) should significantly reduce airmass dependencies

caused by global error terms (e.g., spectroscopic errors) and the overall bias. This will not be perfect, of course, and the results will likely contain a residual latitude-dependent seasonal bias. Once the TCCON priors are used for the ACOS-GOSAT retrievals, the discrepancies caused by the a priori profiles will be eliminated, leaving us only to consider the smoothing error. For the remainder of this paper, only the adjustments in Eq. (4) are applied.

5 Comparisons in the Northern Hemisphere

The first step in evaluating the Northern Hemisphere seasonal cycles from the ACOS-GOSAT data before and after applying Eq. (4) is to inspect the retrieved values in latitude bands corresponding to TCCON sites. Figure 9 shows latitude bands containing the 11 TCCON sites used in this study. The Tsukuba TCCON data were adjusted up by 1.32 ppm in this analysis, due to a known instrumental bias that has been characterized through aircraft calibration campaigns (Tanaka et al., 2011).

The seasonal cycle shape, after applying Eq. (4) to the ACOS-GOSAT data, is generally improved over the data that has only the global bias removed (0.982). Site-by-site investigations require stricter coincidence criteria. However, criteria based on tight geographic and temporal constraints result in few coincidences at higher latitude sites, because the surface is covered in snow, or it is often cloudy.

We can loosen geographic and temporal constraints on the coincidence criteria if we exploit the relationship between the free-tropospheric potential temperature and variability in X_{CO_2} in the Northern Hemisphere (Fig. 10). Keppel-Aleks et al. (2011) detail the use of the potential temperature coordinate as a proxy for equivalent latitude for CO_2 gradients in the Northern Hemisphere. We use the mid-tropospheric temperature field at 700 hPa, T_{700} (which is directly proportional to the potential temperature at 700 hPa for the range of temperatures of interest here), to allow a significantly broader comparison between TCCON and ACOS-GOSAT than could be found using only geographic coincidence. The pressure (700 hPa) is arbitrary, and any mid-tropospheric pressure would do. Choosing 700 hPa is convenient, however, because the NCEP/NCAR analysis product is provided on a 700 hPa grid level (Kalnay et al., 1996), and the NCEP/NCAR data provide the a priori atmospheric information to the TCCON retrieval algorithm. A Northern Hemisphere map of the NCEP/NCAR T_{700} field for 10 days in August 2010 is shown in Fig. 11.

For our coincidence criteria, we find GOSAT measurements within 10 days, latitudes within $\pm 10°$ and longitudes within $\pm 30°$ of the TCCON site, for which T_{700} is ± 2 K of the value over the TCCON site. The longitude limits for Tsukuba are set to be $\pm 10°$ because we do not wish to inadvertently over-weight the measurements over China. The possible locations of the coincidences for each TCCON site, given the latitude, longitude, and T_{700} of each site, are overlaid on the map in Fig. 11. This set of criteria results in many more coincident measurements over the higher latitude sites (Table 3). For example, over Park Falls, the T_{700} criterion results in 10 times more coincident measurements than using a geographic constraint of $\pm 0.5°$ latitude and $\pm 1.5°$ longitude.

These criteria are applied to generate Fig. 12 and Table 3, which show the site-by-site comparisons in the Northern Hemisphere. The correlations between TCCON and ACOS-GOSAT are shown in Fig. 13. All slopes are quoted as $x \pm y$, where x is the best fit slope and y is twice the standard error on the best fit, calculated using the method outlined in York et al. (2004), under the assumption that there is no correlation between the errors in x and the errors in y. The slope is significantly improved after applying Eq. (4) (compare the left and middle panels of Fig. 13, which have slopes of 0.82 ± 0.07 and 0.88 ± 0.07, respectively). Selecting a T_{700} coincidence criterion also improves the coefficient of determination (r^2) over a simple latitude/longitude/time coincidence (compare the middle and right panels of Fig. 13, which have r^2 of 0.80 and 0.77, respectively). When using a T_{700} constraint of ± 1 K (instead of ± 2 K), the r^2 decreases, and the comparison dataset diminishes significantly (10 % loss in data over Park Falls, and 25 % loss in data over Tsukuba). A constraint of ± 3 K shows no reduction in r^2, but also no significant gain in coincident measurements, as the geographic constraints become dominant. Using a simple geographic constraint but with a larger $\pm 2.5°$ box around each TCCON site results in a reduced slope (0.89±0.04) compared with the right panel of Fig. 13 (which has a slope of 0.96 ± 0.08), and the same coefficient of determination ($r^2 = 0.76$).

The variability of the ACOS-GOSAT X_{CO_2} seen in this work is comparable to that described by Morino et al. (2011) and Butz et al. (2011). Morino et al. (2011) remove a large-scale spectroscopic bias that is similar in magnitude to the bias seen in the ACOS retrievals (-8.6ppm, or 2.2%), but a significantly smaller northern hemisphere standard deviation of 1.2 ppm for Białystok, Orléans, Garmisch, Park Falls, Lamont and Tsukuba, using $\pm 2°$ latitude and longitude and ± 1-hour coincidence criteria (Table A1 of Morino et al. (2011)). The ACOS-GOSAT retrievals using the geographic constraint show a variability of 2.6 ppm for these sites (2.2 ppm if using the T_{700} coincidence). The discrepancy may be partly due to the number of soundings used in the Morino et al. (2011) work, which is significantly lower than this work. Butz et al. (2011) have a much smaller large-scale spectroscopic bias (0.45% in the southern hemisphere), because they scale the O_2 A-band absorption cross-sections by 1.030. Their northern hemisphere standard deviation for a $\pm 2.5°$ latitude/longitude box around the TCCON stations (at Białystok, Orléans, Park Falls and Lamont) is 2.55 ppm (from Fig. 2 of Butz et al. (2011), which is very similar to our 2.4 ppm for the same sites (for either the geographic or T_{700} coincidence). The number of coincident spectra in the Butz et al. (2011) work is similar to the geographic constraint in this work.

The correlation slope between the ACOS-GOSAT and TCCON data is not unity within the uncertainty: it is 0.88 ± 0.07 with an r^2 of 0.80. This difference from unity may be partially due to a time-dependent difference in X_{CO_2} between the TCCON data and the ACOS-GOSAT data (Hiroshi Suto, personal communication). This could imply that there is a residual radiometric calibration error (due to degradation of the mirrors or other optical components) or another time-dependent effect, such as a drift in the reference laser frequency. A residual airmass-dependent error remains, especially at very high airmasses, and indeed the assumed linear regression reduces the agreement at very

high airmasses. This is clear in the Eureka time series and in Table 3. Limiting the correlation plot to airmasses $\leq$3.3 improves the r^2 and increases the slope (to 0.85 and 0.93 ± 0.08, respectively). The additional airmass-dependent errors may be reduced by adjusting the ACOS-GOSAT retrieval to the TCCON a priori profile and accounting for the photosynthetic fluorescence signal. OCO-2's target mode will allow for a determination of the airmass dependence globally.

Even after modification of the ACOS-GOSAT data by Eq. (4), the ACOS-GOSAT noise is too large to see significant (~ 2 ppm) interannual X_{CO_2} drawdown differences. Figure 10 shows the relationship between ΔX_{CO_2} and T_{700} in the Northern Hemisphere for 2009 and 2010. The mean standard deviation of the ACOS-GOSAT data plotting in Figure 10 in August 2009 (2010) is 2.5 ppm (2.9 ppm), and the mean standard deviation of the ACOS-GOSAT data in December 2009 (2010) is 3.7 ppm (3.4 ppm). Although the range of potential temperatures sampled at the TCCON sites differs substantially between 2009 and 2010 (because the Eureka and Sodankylä sites were not yet recording X_{CO_2} data), all TCCON sites operating in both 2009 and 2010 show a stronger ΔX_{CO_2} drawdown (2–3 ppm) in August 2009 than in 2010. This interannual difference is indistiguishable in the ACOS-GOSAT data, as it is within its noise (plotted as 1σ error bars). As further improvements to the ACOS algorithms are implemented, the noise should reduce, and we anticipate that these important interannual features will become separable from the noise.

6 Discussion and conclusions

Estimating sources of bias in satellite observations is essential if the data are to be used to infer surface fluxes. The ACOS retrievals of X_{CO_2} from the GOSAT TANSO-FTS instrument contain global and regional systematic errors. We have demonstrated that bias between the ACOS-GOSAT retrieval of X_{CO_2} data and TCCON X_{CO_2} is significantly reduced if a set of modifications determined from the Southern Hemisphere data is applied globally. After applying the modifications to the data described by Eq. (4), the comparisons of ACOS-GOSAT X_{CO_2} to TCCON are significantly improved but remain imperfect and show both residual time and airmass dependences. Future versions of the ACOS-GOSAT data will include an updated radiometric calibration, a fluorescence correction and a nonlinearity correction, and will use a seasonally and latitudinally varying a priori profile, all of which should improve the retrievals.

One underlying assumption in this work has been that the X_{CO_2} gradients in the Southern Hemisphere are small. We expect that as the quality of the satellite data improves, this assumption will become less valid. In future work, using assimilations of Southern Hemisphere CO_2 (e.g., CarbonTracker, described by Peters et al., 2007) and the Southern Hemisphere TCCON sites could provide a more robust estimate of the true Southern Hemisphere X_{CO_2} fields. A second important assumption we have made is that the spurious variability in the Northern Hemisphere is caused by the same retrieval or instrument parameters that cause the spurious variability in the Southern Hemisphere.

Anywhere that this assumption is invalid will lead to residual variability and bias in the Northern Hemisphere.

When turning to comparisons of ACOS-GOSAT X_{CO_2} with TCCON in the Northern Hemisphere, coincidence criteria that include the temperature at 700 hPa, which serves as a tracer of dynamically-driven variability in X_{CO_2}, allow for a broader comparison with larger sample sizes. The ACOS-GOSAT noise in v2.8 is still too large to distinguish interannual variability in the Northern Hemisphere seasonal cycles in 2009 and 2010, but we anticipate that future versions of the ACOS algorithm will be able to clearly distinguish the two years.

The methods outlined in this paper: using the Southern Hemisphere to define modifications to remove spurious variability, and using the temperature at 700 hPa to define coincidence criteria in the Northern Hemisphere, are readily applicable to other satellite instruments observing X_{CO_2}. These methods are directly applicable to the future OCO-2 retrieval algorithm, and will form the basis for initial evaluations of the OCO-2 data.

Appendix A

The effect of averaging kernels

The averaging kernels and a priori profiles for the ACOS-GOSAT retrievals over Lamont and the TCCON FTS retrievals are shown in Figs. A1 and A2. According to Rodgers and Connor (2003), to compare retrieval results from two different instruments with differing viewing geometries, retrieval algorithms, a priori profiles ($\boldsymbol{x}_{\mathrm{a}}$) and averaging kernels ($\mathbf{A}$), an "ensemble" profile ($\boldsymbol{x}_{\mathrm{c}}$) and covariance matrix ($\mathbf{S}_{\mathrm{c}}$) should be selected, which represent the mean and variability of the ensemble of true atmospheric profiles over which the comparison is to be made. That is, in order to compare retrieved values $\hat{\boldsymbol{x}}_i$ from the i-th instrument, the equations, traditionally written as

$$\hat{\boldsymbol{x}}_i - \boldsymbol{x}_{\mathrm{a}i} = \mathbf{A}_i(\boldsymbol{x} - \boldsymbol{x}_{\mathrm{a}i}) + \boldsymbol{\epsilon}_{xi} \tag{A1}$$

with measurement error $\boldsymbol{\epsilon}_{xi}$, should be "adjusted" to a common comparison ensemble, $\boldsymbol{x}_{\mathrm{c}}$, by adding $(\mathbf{A}_i - \mathbf{I})(\boldsymbol{x}_{\mathrm{a}i} - \boldsymbol{x}_{\mathrm{c}})$ to both sides of the equation, giving our new, adjusted equations:

$$\hat{\boldsymbol{x}}_i' - \boldsymbol{x}_{\mathrm{c}} = \mathbf{A}_i(\boldsymbol{x} - \boldsymbol{x}_{\mathrm{c}}) + \boldsymbol{\epsilon}_{xi} \tag{A2}$$

where $\hat{\boldsymbol{x}}_i'$ is the "adjusted" $\hat{\boldsymbol{x}}$, and $\mathbf{I}$ is the identity matrix:

$$\hat{\boldsymbol{x}}_i' \equiv \hat{\boldsymbol{x}}_i + (\mathbf{A}_i - \mathbf{I})(\boldsymbol{x}_{\mathrm{a}i} - \boldsymbol{x}_{\mathrm{c}}) \tag{A3}$$

We are interested in comparing the dry-air mole fractions (DMFs, X_{CO_2}) in ppm, and not the profiles of CO_2. The X_{CO_2} are computed by dividing the total column abundances of CO_2 by the column of dry air.

$$X_{CO_2} = \frac{\text{column } CO_2}{\text{column dry air}} \tag{A4}$$

The column of dry air can be computed in two ways: directly using a measurement of the O_2 column, and using the surface pressure (P_{surf}) corrected for the H_2O column:

$$\text{column dry air} = \frac{\text{column } O_2}{0.2095} \tag{A5}$$

$$= \frac{P_{\mathrm{surf}}}{\{g\}_{\mathrm{air}} m_{\mathrm{air}}^{\mathrm{dry}}} - \mathrm{column}_{\mathrm{H_2O}} \frac{m_{\mathrm{H_2O}}}{m_{\mathrm{air}}^{\mathrm{dry}}} \tag{A6}$$

where $m_{\mathrm{H_2O}}$ is the molecular weight of water ($18.02 \times 10^{-3}/N_{\mathrm{A}}$ kg molecule^{-1}), $m_{\mathrm{air}}^{\mathrm{dry}}$ is the molecular weight of dry air ($28.964 \times 10^{-3}/N_{\mathrm{A}}$ kg molecule^{-1}), N_{A} is Avogadro's constant, and $\{g\}_{\mathrm{air}}$ is the column-averaged gravitational acceleration.

The TCCON and ACOS-GOSAT algorithms compute the total column of dry air in different ways. Both use a measurement of the O_2 column, but the TCCON approach is to divide the total column of CO_2 by the total column of O_2, measured in the 1.27 µm spectral region (i.e., Eq. A5). This approach is advantageous because the CO_2 and O_2 bands are spectrally close, so many errors caused by instrumental imperfections are reduced in the ratio, and no additional water vapor correction is necessary (Wallace and Livingston, 1990; Yang et al., 2002; Wunch et al., 2011). Mesospheric dayglow from the 1.27 µm O_2 band precludes useful measurements of this band from space, and so the GOSAT instrument measures the O_2 A-band (0.76 µm). The ACOS-GOSAT algorithm cannot simply use the TCCON formulation (Eq. A5) because the A-band is spectrally distant from the CO_2 bands and is measured on a separate detector. Instead, it uses the O_2 A-band measurements to compute a surface pressure, which is then used to compute the dry air column via Eq. (A6), explicitly correcting for the water column with the retrieved value from the ACOS algorithm.

The retrieved X_{CO_2}, denoted $\hat{c}$, can also be described as the profile-weighted column-average CO_2 mixing ratio in dry air, and is related to the retrieved profile, $\hat{\boldsymbol{x}}$, via the pressure weighting function $\boldsymbol{h}$, described by Connor et al. (2008).

$$\hat{c} = \boldsymbol{h}^T \hat{\boldsymbol{x}} \tag{A7}$$

The pressure weighting function contains the pressure thicknesses in the state vector, normalized by the surface pressure corrected for the atmospheric water content. Applying $\boldsymbol{h}^T = (h_1, ..., h_j, ...)$ to both sides of Eq. (A2) gives Eq. (22) in Rodgers and Connor (2003):

$$\hat{c}_i' - c_{\mathrm{c}} = \boldsymbol{h}^T \mathbf{A}_i (\boldsymbol{x} - \boldsymbol{x}_{\mathrm{c}}) + \epsilon_{\mathrm{c}i} = \sum_j h_j a_{ij} (\boldsymbol{x} - \boldsymbol{x}_{\mathrm{c}})_j + \epsilon_{\mathrm{c}i}, \tag{A8}$$

where $\epsilon_{\mathrm{c}i}$ is the measurement error on the column retrieval for instrument i and j is the pressure level. The normalized column averaging kernel is $\boldsymbol{a}_i = (a_{i1}, ..., a_{ij}, ...)^T$ for instrument i and is defined by Connor et al. (2008), Eq. (8):

$$a_{ij} = \frac{\partial \hat{c}_i}{\partial x_j} \frac{1}{h_j} = \left(\boldsymbol{h}^T \mathbf{A}_i\right)_j \frac{1}{h_j} \tag{A9}$$

The "adjusted" retrieved column $\hat{c}_i'$ is then

$$\hat{c}_i' \equiv \hat{c}_i + \sum_j h_j (\boldsymbol{a}_i - \boldsymbol{u})_j (\boldsymbol{x}_{\mathrm{a}i} - \boldsymbol{x}_{\mathrm{c}})_j \tag{A10}$$

where $\boldsymbol{u}$ is a vector of ones. The difference and variance in the DMFs are then represented by Eqs. (23) and (24) from Rodgers and Connor (2003):

$$\hat{c}_1' - \hat{c}_2' = \sum_j h_j (\boldsymbol{a}_1 - \boldsymbol{a}_2)_j (\boldsymbol{x} - \boldsymbol{x}_\mathrm{c})_j + \epsilon_{\mathrm{c}1} + \epsilon_{\mathrm{c}2} \tag{A11}$$

$$\sigma^2 (\hat{c}_1' - \hat{c}_2') = \sum_k \sum_j h_j (\boldsymbol{a}_1 - \boldsymbol{a}_2)_j (\mathbf{S}_\mathrm{c})_{jk} h_k (\boldsymbol{a}_1 - \boldsymbol{a}_2)_k + \sigma_{\mathrm{c}1}^2 + \sigma_{\mathrm{c}2}^2 \tag{A12}$$

The matrix $\mathbf{S}_\mathrm{c}$ is the ensemble covariance matrix, and represents the real atmospheric variability. We will use the convention that GOSAT is $i = 1$, and TCCON is $i = 2$.

For simplicity, we can choose the TCCON a priori profile as the ensemble profile (e.g., $\boldsymbol{x}_{\mathrm{a}2} = \boldsymbol{x}_\mathrm{c}$). The TCCON a priori profile is a statistically reasonable estimate of $\mathrm{X}_{\mathrm{CO}_2}$ in the atmosphere – it is an empirical function that is latitude- and time-dependent, built on the GLOBALVIEW data set in the troposphere (GLOBALVIEW-CO_2, 2006) and the age-of-air calculations of Andrews et al. (2001) in the stratosphere.

If the first term on the right hand side of Eq. (A12) is small compared with $\sigma_{\mathrm{c}1}^2 + \sigma_{\mathrm{c}2}^2$, then an adjustment to a common ensemble a priori profile is sufficient to account for the major differences in the two retrievals at the same location and time. This means that we can directly compare $\hat{c}_1'$ and $\hat{c}_2'$.

However, if the first term on the right hand side of Eq. (A12) is not negligibly small, we must reduce our smoothing error by computing what the GOSAT instrument would retrieve given the TCCON total column as "truth," via Eq. (25) from Rodgers and Connor (2003):

$$\hat{c}_{12}' = c_\mathrm{c} + \sum_j h_j a_{1j} (\hat{\boldsymbol{x}}_2 - \boldsymbol{x}_\mathrm{c})_j = c_\mathrm{c} + \sum_j h_j a_{1j} (\gamma \boldsymbol{x}_\mathrm{c} - \boldsymbol{x}_\mathrm{c})_j \tag{A13}$$

where γ is the TCCON scaling factor applied to the a priori profile to get the final TCCON profile that is then integrated to produce $\hat{c}_2$.

A comparison of $\hat{c}_{12}'$ with $\hat{c}_1'$ (the GOSAT adjusted retrieval) should significantly reduce the smoothing error introduced by the averaging kernels. Analogs of Eqs. (A11) and (A12) for this case are found in Eqs. (26) and (27) of Rodgers and Connor (2003):

$$\hat{c}_1 - \hat{c}_{12} = \sum_j h_j a_{1j} ((\mathbf{I} - \mathbf{A}_2)(\boldsymbol{x} - \boldsymbol{x}_\mathrm{c}))_j + \epsilon_{\mathrm{c}1} - \sum_j h_j a_{1j} \epsilon_{x2j} \tag{A14}$$

$$\begin{aligned} \sigma^2 (\hat{c}_1 - \hat{c}_{12}) = & \sum_k \sum_j h_j a_{1j} \left((\mathbf{I} - \mathbf{A}_2) \mathbf{S}_\mathrm{c} (\mathbf{I} - \mathbf{A}_2)^T \right)_{jk} h_k a_{1k} + \sigma_{\mathrm{c}1}^2 \\ & + \sum_k \sum_j h_j a_{1j} (\mathbf{S}_{x2})_{jk} h_k a_{1k} \end{aligned} \tag{A15}$$

A full profile (from the surface up to 12 km) was measured by an instrumented aircraft over Lamont on 2 August 2009, which provides an example "true" profile (i.e., $\boldsymbol{x}$). Using this profile to compute $(\boldsymbol{a}_1 - \boldsymbol{a}_2)^T (\boldsymbol{x} - \boldsymbol{x}_\mathrm{c})$ yields a difference of about 0.2 ppm, which is very small compared with $\epsilon_1 + \epsilon_2 \approx 2.3$ ppm. Figure A3 shows the profiles and averaging kernels used in the calculation above.

Appendix B

A Preview of ACOS v2.9

A significant subset of version 2.9 data, covering July 1, 2009 through March 28, 2011, has been processed since this paper was first published. Significant changes and improvements to the algorithm include

- **The new time dependence of the radiometric calibration was computed and applied to the data and noise model.** This implies that the time-dependent filter on the χ^2 values described in Table 1 is no longer necessary. The new recommendation for the χ^2 filters is described in Table B1.
- **The $\mathbf{O_2}$ A-band cross-sections were scaled by 1.024.** This has corrected the $\sim$11 hPa bias between the retrieved surface pressure and the ECMWF surface pressure. This also eliminates the need for the overall bias correction factor (0.982 in v2.8).
- **The zero level offsets in the $\mathbf{O_2}$ A-band were removed through fitting the spectra with an additional parameter.** This reduces the error caused by detector nonlinearity, improves the spectral fits and should have some impact on the relationship between $\mathrm{X_{CO_2}}$ and both signal_o2 and airmass.
- **The stratospheric column averaging kernel has been corrected.** This should have little impact on the retrieved $\mathrm{X_{CO_2}}$, and was a bug in the pressure-weighting function calculation.

The a priori profiles remain unchanged and fluorescence has not yet been included in the state vector. Hence, there may still be both a latitude-dependent seasonal cycle induced by the a priori profile (compared with using the more realistic TCCON a priori), and continued signal_o2 dependencies due to the unaccounted fluorescence signal in the $\mathrm{O_2}$ A-band.

Using the v2.9 soundings to investigate the relationships described in §4, we have determined that the same four parameters (blended albedo, ΔP, airmass and signal_o2) remain important, and the new coefficients for Assumption 1 are: $C_0 = 1.00$, $C_1 = 6.5 \pm 0.4$ ppm/units of blended albedo, $C_2 = -0.15 \pm 0.01$ ppm hPa^{-1}, $C_3 = -1.3 \pm 0.4$ ppm/airmass, and $C_4 = -0.47 \pm 0.08$ ppm/(10^7 Wcm^{-2}sr^{-1} (cm^{-1})$^{-1}$). The blended albedo and signal_o2 coefficients are statistically significantly different from those computed from the v2.8 data. The v2.9 data exhibit smaller biases and comparable random noise to the v2.8 data (Table B2). The resulting slopes for the equivalent of Figure 13 are closer to 1 than in v2.8, and are well within error of 1 after modification by equation 4 with the coefficients described above (0.98 ± 0.07, Fig. B1).

We now have more confidence in our glint data in v2.9, and would encourage data users to use it with caution. The parameters that are used to minimize the variance in the southern hemisphere glint data will likely not be the same as those needed to modify the land data. It is useful to note that the

glint flag in the v2.9 data is incorrect after mid-October, 2010, when the GOSAT viewing strategy changed from a 5-point observation to a 3-point observation. A suitable glint flag is described in Table B1. When using both glint and nadir data to determine the fit parameters in equation 4, the coefficients change significantly. The covariates for calculating a bias in the glint data will be different from those used for the land data, because there are no glint data poleward of 25°S between March and October, and there is little variability in airmass and signal_o2. The overall difference between the glint and glint-free data in the Southern Hemisphere over the same time period is ~ 1 ppm.

Acknowledgements. The authors wish to thank Sergey Oshchepkov, Peter Rayner, editor Ilse Aben and an anonymous reviewer for insightful and constructive comments and suggestions. We had helpful discussions with Hiroshi Suto (JAXA) about the apparent time-dependent drift in the ACOS-GOSAT data. GOSAT spectra were kindly provided to the California Institute of Technology through an RA agreement with JAXA, NIES and the MOE. US funding for TCCON comes from NASA's Terrestrial Ecology Program, grant number NNX11AG01G, the Orbiting Carbon Observatory Program, the Atmospheric CO_2 Observations from Space (ACOS) Program and the DOE/ARM Program. The Darwin TCCON site was built at Caltech with funding from the OCO project, and is operated by the University of Wollongong, with travel funds for maintenance and equipment costs funded by the OCO-2 project. We acknowledge funding to support Darwin and Wollongong from the Australian Research Council, Projects LE0668470, DP0879468, DP110103118 and LP0562346. Lauder TCCON measurements are funded by New Zealand Foundation of Research Science and Technology contracts C01X0204 and CO1X0406. We acknowledge financial support of the Białystok and Orléans TCCON sites from the Senate of Bremen and EU projects IMECC and GEOmon as well as maintenance and logistical work provided by AeroMeteo Service (Białystok) and the RAMCES team at LSCE (Gif-sur-Yvette, France). The PEARL Bruker 125HR measurements at Eureka were made by the Canadian Network for the Detection of Atmospheric Change (CANDAC), led by James R. Drummond, and in part by the Canadian Arctic ACE Validation Campaigns, led by Kaley A. Walker. They were supported by the Atlantic Innovation Fund/Nova Scotia Research Innovation Trust, Canada Foundation for Innovation, Canadian Foundation for Climate and Atmospheric Sciences, Canadian Space Agency, Environment Canada, Government of Canada International Polar Year funding, Natural Sciences and Engineering Research Council, Northern Scientific Training Program, Ontario Innovation Trust, Polar Continental Shelf Program, and Ontario Research Fund. The authors wish to thank Rebecca Batchelor and Ashley Harrett for the near-infrared upgrade of the instrument, PEARL site manager Pierre Fogal, the staff at the Eureka weather station, and the CANDAC operators for the logistical and on-site support provided at Eureka. Part of this work was performed at the Jet Propulsion Laboratory, California Institute of Technology, under contract with NASA. NCEP Reanalysis data is provided by the NOAA/OAR/ESRL PSD, Boulder, Colorado, USA, from their Web site at http://www.cdc.noaa.gov/.

References

Abrams, M., Toon, G., and Schindler, R.: Practical example of the correction of Fourier-transform spectra for detector nonlinearity, Appl. Optics, 33, 6307–6314, 1994.

ACOS-GOSAT Data Access: http://disc.sci.gsfc.nasa.gov/acdisc/data-holdings/acos-data-holdings, last access July 2011.

Andrews, A., Boering, K., Daube, B., Wofsy, S., Loewenstein, M., Jost, H., Podolske, J., Webster, C., Herman, R., Scott, D., Flesch, G. J., Moyer, E. J., Elkins, J. W., Dutton, G. S., Hurst, D. F., Moore, F. L., Ray, E. A., Romashkin, P. A., and Strahan, S. E.: Mean ages of stratospheric air derived from in situ observations of CO_2, CH_4, and N_2O, J. Geophys. Res.-Atmos., 106, 32295–32314, 2001.

Boesch, H., Toon, G., Sen, B., Washenfelder, R., Wennberg, P., Buchwitz, M., De Beek, R., Burrows, J., Crisp, D., Christi, M., Connor, B. J., Natraj, V., and Yung, Y. L.: Space-based near-infrared CO2 measurements: Testing the Orbiting Carbon Observatory retrieval algorithm and validation concept using SCIAMACHY observations over Park Falls, Wisconsin, J. Geophys. Res., 111, 0148–0227, 2006.

Boesch, H., Baker, D., Connor, B., Crisp, D., and Miller, C.: Global Characterization of CO2 Column Retrievals from Shortwave-Infrared Satellite Observations of the Orbiting Carbon Observatory-2 Mission, Remote Sensing, 3, 270–304, http://dx.doi.org/10.3390/rs3020270doi:10.3390/rs3020270, http://www.mdpi.com/2072-4292/3/2/270/, 2011.

Burrows, J. P., Hölzle, E., Goede, A. P. H., Visser, H., and Fricke, W.: SCIAMACHY–scanning imaging absorption spectrometer for atmospheric chartography, Acta Astronautica, 35, 445–451, http://dx.doi.org/10.1016/0094-5765(94)00278-Tdoi:10.1016/0094-5765(94)00278-T, http://www.sciencedirect.com/science/article/pii/009457659400278T, earth Observation, 1995.

Butz, A., Guerlet, S., Hasekamp, O., Schepers, D., Galli, A., Aben, I., Frankenberg, C., Hartmann, J.-M., Tran, H., Kuze, A., Keppel-Aleks, G., Toon, G., Wunch, D., Wennberg, P., Deutscher, N., Griffith, D., Macatangay, R., Messerschmidt, J., Notholt, J., and Warneke, T.: Toward accurate CO_2 and CH_4 observations from GOSAT, Geophys. Res. Lett., 38, L14812, http://dx.doi.org/10.1029/2011GL047888doi:10.1029/2011GL047888, 2011.

Connor, B., Boesch, H., Toon, G., Sen, B., Miller, C., and Crisp, D.: Orbiting Carbon Observatory: Inverse method and prospective error analysis, J. Geophys. Res., 113, D05305, http://dx.doi.org/10.1029/2006JD008336doi:10.1029/2006JD008336, 2008.

Conway, T. and Tans, P.: NOAA/ESRL, www.esrl.noaa.gov/gmd/ccgg/trends/, accessed 1 June 2011.

Deutscher, N. M., Griffith, D. W. T., Bryant, G. W., Wennberg, P. O., Toon, G. C., Washenfelder, R. A., Keppel-Aleks, G., Wunch, D., Yavin, Y., Allen, N. T., Blavier, J.-F., Jiménez, R., Daube, B. C., Bright, A. V., Matross, D. M., Wofsy, S. C., and Park, S.: Total column CO_2 measurements at Darwin, Australia – site description and calibration against in situ aircraft profiles, Atmos. Meas. Tech., 3, 947–958, http://dx.doi.org/10.5194/amt-3-947-2010doi:10.5194/amt-3-947-2010, 2010.

Efron, B. and Gong, G.: A Leisurely Look at the Bootstrap, the Jackknife, and Cross-Validation, The American Statistician, 37, pp. 36–48, http://www.jstor.org/stable/2685844, 1983.

Frankenberg, C., Butz, A., and Toon, G. C.: Disentangling chlorophyll fluorescence from atmospheric scattering effects in O2A-band spectra of reflected sun-light, Geophys. Res. Lett., 38, L03801, http://dx.doi.org/10.1029/2010GL045896doi:10.1029/2010GL045896, 2011.

GLOBALVIEW-CO_2: Cooperative Atmospheric Data Integration Project – Carbon Dioxide, CD-ROM, NOAA GMD, Boulder, Colorado, 2006.

Hamazaki, T., Kaneko, Y., Kuze, A., and Kondo, K.: Fourier transform spectrometer for greenhouse gases observing satellite (GOSAT), in: Proceedings of SPIE, vol. 5659, p. 73, 2005.

Hartmann, J.-M., Tran, H., and Toon, G. C.: Influence of line mixing on the retrievals of atmospheric CO_2 from spectra in the 1.6 and 2.1 µm regions, Atmos. Chem. Phys., 9, 7303–7312, http://dx.doi.org/10.5194/acp-9-7303-2009doi:10.5194/acp-9-7303-2009, 2009.

Joiner, J., Yoshida, Y., Vasilkov, A. P., Yoshida, Y., Corp, L. A., and Middleton, E. M.: First observations of global and seasonal terrestrial chlorophyll fluorescence from space, Biogeosciences, 8, 637–651, http://dx.doi.org/10.5194/bg-8-637-2011doi:10.5194/bg-8-637-2011, 2011.

Kalnay, E., Kanamitsu, M., Kistler, R., Collins, W., Deaven, D., Gandin, L., Iredell, M., Saha, S., White, G., Woollen, J., Zhu, Y., Leetmaa, A., Reynolds, B., Chelliah, M., Ebisuzaki, W., Higgins, W., Janowiak, J., Mo, K. C., Ropelewski, C., Wang, J., Jenne, R., and Joseph, D.: The NCEP/NCAR 40-year reanalysis project, B. Am. Meteorol. Soc., 77, 437–471, 1996.

Keppel-Aleks, G., Wennberg, P. O., and Schneider, T.: Sources of variations in total column carbon dioxide, Atmos. Chem. Phys., 11, 3581–3593, http://dx.doi.org/10.5194/acp-11-3581-2011doi:10.5194/acp-11-3581-2011, 2011.

Long, D., Havey, D., Okumura, M., Miller, C., and Hodges, J.: O_2 A-band line parameters to support atmospheric remote sensing, J. Quant. Spectr. Radiat. T., 111, 2021–2036, 2010.

Messerschmidt, J., Geibel, M. C., Blumenstock, T., Chen, H., Deutscher, N. M., Engel, A., Feist, D. G., Gerbig, C., Gisi, M., Hase, F., Katrynski, K., Kolle, O., Lavrič, J. V., Notholt, J., Palm, M., Ramonet, M., Rettinger, M., Schmidt, M., Sussmann, R., Toon, G. C., Truong, F., Warneke, T., Wennberg, P. O., Wunch, D., and Xueref-Remy, I.: Calibration of TCCON column-averaged CO_2: the first aircraft campaign over European TCCON sites, Atmos. Chem. Phys. Discuss., 11, 14541–14582, http://dx.doi.org/10.5194/acpd-11-14541-2011doi:10.5194/acpd-11-14541-2011, 2011.

Morino, I., Uchino, O., Inoue, M., Yoshida, Y., Yokota, T., Wennberg, P. O., Toon, G. C., Wunch, D., Roehl, C. M., Notholt, J., Warneke, T., Messerschmidt, J., Griffith, D. W. T., Deutscher, N. M., Sherlock, V., Connor, B., Robinson, J., Sussmann, R., and Rettinger, M.: Preliminary validation of column-averaged volume mixing ratios of carbon dioxide and methane retrieved from GOSAT short-wavelength infrared spectra, Atmos. Meas. Tech., 4, 1061–1076, http://dx.doi.org/10.5194/amt-4-1061-2011doi:10.5194/amt-4-1061-2011, 2011.

Natraj, V. and Spurr, R.: A fast linearized pseudo-spherical two orders of scattering model to account for polarization in vertically inhomogeneous scattering-absorbing media, J. Quant. Spectr. Radiat. T., 107, 263–293, 2007.

O'Brien, D., Polonsky, I., O'Dell, C., and Cardehen, A.: Orbiting Carbon Observatory (OCO) algorithm theoretical basis document: The OCO simulator, Cooperative Institute for Research in the Atmosphere, Colorado State University, Tech. Rep. ISSN, pp. 0737–5352, 2009.

O'Dell, C.: Acceleration of multiple-scattering, hyperspectral radiative transfer calculations via low-streams interpolation, J. Geophys. Res., 115, D10206, http://dx.doi.org/10.1029/2009JD012803doi:10.1029/2009JD012803, 2010.

O'Dell, C. W., Connor, B., Bösch, H., O'Brien, D., Frankenberg, C., Castano, R., Christi, M., Crisp, D., Eldering, A., Fisher, B., Gunson, M., McDuffie, J., Miller, C. E., Natraj, V., Oyafuso, F., Polonsky, I., Smyth, M., Taylor, T., Toon, G. C., Wennberg, P. O., and Wunch, D.: The ACOS CO_2 retrieval algorithm – Part 1: Description and validation against synthetic observations, Atmos. Meas. Tech. Discussions, 4, 5, 6097–6158, http://www.atmos-meas-tech-discuss.net/4/6097/2011/doi:10.5194/amtd-4-6097-2011, 2011.

Olsen, S. and Randerson, J.: Differences between surface and column atmospheric CO_2 and implications for carbon cycle research, J. Geophys. Res., 109, D02301, http://dx.doi.org/10.1029/2003JD003968doi:10.1029/2003JD003968, 2004.

Parker, R., Boesch, H., Cogan, A., Fraser, A., Feng, L., Palmer, P.I., Messerschmidt, J., Deutscher, N., Griffith, D.W.T., Notholt, J. , Wennberg, P.O., and Wunch, D.: Methane observations from the Greenhouse Gases Observing SATellite: Comparison to ground-based TCCON data and model calculations, Geophysical Research Letters, 38, L15807, 2011.

Peters, W., Jacobson, A., Sweeney, C., Andrews, A., Conway, T., Masarie, K., Miller, J., Bruhwiler, L., Pétron, G., Hirsch, A., Worthy, D. E. J., van der Werf, G. R., Randerson, J. T., Wennberg, P. O., Krol, M. C., and Tans, P. P.: An atmospheric perspective on North American carbon dioxide exchange: CarbonTracker, Proc. Natl. Acad. Sci., 104, 18925–18930, 2007.

Rodgers, C.: Inverse methods for atmospheric sounding: Theory and practice, World Scientific Singapore, 2000.

Rodgers, C. and Connor, B.: Intercomparison of remote sounding instruments, J. Geophys. Res, 108, 4116–4229, 2003.

Rothman, L., Gordon, I., Barbe, A., Benner, D., Bernath, P., Birk, M., Boudon, V., Brown, L., Campargue, A., Champion, J., Chance, K., Coudert, L. H., Dana, V., Devi, V. M., Fally, S., Flaud, J.-M., Gamache, R. R., Goldman, A., Jacquemart, D., Kleiner, I., Lacome, N., Lafferty, W. J., Mandin, J.-Y., Massie, S. T., Mikhailenko, S. N., Miller, C. E., Moazzen-Ahmadi, N., Naumenko, O. V., Nikitin, A. V., Orphal, J., Perevalov, V. I., Perrin, A., Predoi-Cross, A., Rinsland, C. P., Rotger, M., Šimečková, M., Smith, M. A. H., Sung, K., Tashkun, S. A., Tennyson, J., Toth, R. A., Vandaele, A. C., and Vander Auwera, J.: The HITRAN 2008 molecular spectroscopic database, J. Quant. Spectr. Radiat. T., 110, 533–572, 2009.

Savtchenko, A. and Avis, C.: README Document for ACOS Level 2 Standard Product, http://disc.sci.gsfc.nasa.gov/acdisc/documentation/ACOS.shtml, 2010.

Spurr, R.: Simultaneous derivation of intensities and weighting functions in a general pseudo-spherical discrete ordinate radiative transfer treatment, J. Quant. Spectr. Radiat. T., 75, 129–175, 2002.

Spurr, R., Kurosu, T., and Chance, K.: A linearized discrete ordinate radiative transfer model for atmospheric remote-sensing retrieval, J. Quant. Spectr. Radiat. T., 68, 689–735, 2001.

Suto, H. and Kuze, A.: Correction of scan-speed instability of TANSO-FTS on GOSAT, Abstract A51C-0107 presented at 2010 Fall Meeting, AGU, San Francisco, Calif., 13–17 December 2010.

Tanaka, T., et al.: The 2010 Aircraft Calibration Campaign over Tsukuba, Japan, in preparation, 2011.

Taylor, T. E., O'Dell, C. W., O'Brien, D. M., Kikuchi, N., Yokota, T., Nakajima, T. Y., Ishida, H., Crisp, D., and Nakajima, T.: Comparison of Cloud-Screening Methods Applied to GOSAT Near-Infrared Spectra, IEEE Transactions on Geoscience and Remote Sensing, 99, 1–15, http://dx.doi.org/10.1109/TGRS.2011.2160270doi:10.1109/TGRS.2011.2160270, 2011.

Toth, R., Brown, L., Miller, C., Malathy Devi, V., and Benner, D.: Spectroscopic database of CO_2 line parameters: 4300–7000 cm^{-1}, J. Quant. Spectr. Radiat. T., 109, 906–921, 2008.

Tran, H. and Hartmann, J.: An improved O_2 A band absorption model and its consequences for retrievals of photon paths and surface pressures, J. Geophys. Res., 113, D18104, http://dx.doi.org/10.1029/2008JD010011doi:10.1029/2008JD010011, 2008.

Wallace, L. and Livingston, W.: Spectroscopic observations of atmospheric trace gases over Kitt Peak. I – Carbon dioxide and methane from 1979 to 1985, J. Geophys. Res., 95, 9823–9827, http://dx.doi.org/10.1029/JD095iD07p09823doi:10.1029/JD095iD07p09823, 1990.

Washenfelder, R., Toon, G., Blavier, J., Yang, Z., Allen, N., Wennberg, P., Vay, S., Matross, D., and Daube, B.: Carbon dioxide column abundances at the Wisconsin Tall Tower site, J. Geophys. Res., 111, D22305, http://dx.doi.org/10.1029/2006JD007154doi:10.1029/2006JD007154, 2006.

Wofsy, S. C., Daube, B. C., Jimenez, R., Kort, E., Pittman, J. V., Park, S., Commane, R., Xiang, B., Santoni, G., Jacob, D., Fisher, J., Pickett-Heaps, C., Wang, H., Wecht, K., Wang, Q.-Q., Stephens, B. B., Schertz, S., Romashkin, P., Campos, T., Haggerty, J., Cooper, W. A., Rogers, D., Beaton, S., Elkins, J. W., Fahey, D., Gao, R., Moore, F., Montzka, S. A., Schwartz, J. P., Hurst, D., Miller, B., Sweeney, C., Oltmans, S., Nance, D., Hintsa, E., Dutton, G., Watts, L. A., Spackman, R., Rosenlof, K., Ray, E., Zondlo, M., Diao, M., Mahoney, M. J., Chahine, M., Olsen, E., Keeling, R., Bent, J., Atlas, E. A., Lueb, R., Patra, P., Ishijima, K., Engelen, R., Nassar, R., Jones, D. B., and Mikaloff-Fletcher, S.: HIAPER Pole-to-Pole Observations (HIPPO): Fine grained, global scale measurements for determining rates for transport, surface emissions, and removal of climatically important atmospheric gases and aerosols, Phil. Trans. R. Soc. A, 369, 2073–2086, http://dx.doi.org/10.1098/rsta.2010.0313doi:10.1098/rsta.2010.0313, 2011.

Wunch, D., Toon, G. C., Wennberg, P. O., Wofsy, S. C., Stephens, B. B., Fischer, M. L., Uchino, O., Abshire, J. B., Bernath, P., Biraud, S. C., Blavier, J.-F. L., Boone, C., Bowman, K. P., Browell, E. V., Campos, T., Connor, B. J., Daube, B. C., Deutscher, N. M., Diao, M., Elkins, J. W., Gerbig, C., Gottlieb, E., Griffith, D. W. T., Hurst, D. F., Jiménez, R., Keppel-Aleks, G., Kort, E. A., Macatangay, R., Machida, T., Matsueda, H., Moore, F., Morino, I., Park, S., Robinson, J., Roehl, C. M., Sawa, Y., Sherlock, V., Sweeney, C., Tanaka, T., and Zondlo, M. A.: Calibration of the Total Carbon Column Observing Network using aircraft profile data, Atmos. Meas. Tech., 3, 1351–1362, http://dx.doi.org/10.5194/amt-3-1351-2010doi:10.5194/amt-3-1351-2010, 2010.

Wunch, D., Toon, G. C., Blavier, J.-F. L., Washenfelder, R., Notholt, J., Connor, B. J., Griffith, D. W. T., Sherlock, V., and Wennberg, P. O.: The Total Carbon Column Observing Network, Phil. Trans. R. Soc. A, 369, 2087–2112, http://dx.doi.org/10.1098/rsta.2010.0240doi:10.1098/rsta.2010.0240, 2011.

Yang, Z., Toon, G., Margolis, J., and Wennberg, P.: Atmospheric CO_2 retrieved from ground-based near IR solar spectra, Geophys. Res. Lett., 29, 53–1, 2002.

Yang, Z., Wennberg, P., Cageao, R., Pongetti, T., Toon, G., and Sander, S.: Ground-based photon path measurements from solar absorption spectra of the O_2 A-band, J. Quant. Spectr. Radiat. T., 90, 309–321, 2005.

Yokota, T., Oguma, H., Morino, I., and Inoue, G.: A nadir looking SWIR FTS to monitor CO_2 column density for Japanese GOSAT project, Proc. Twenty-fourth Int. Sympo. on Space Technol. and Sci.(Selected Papers), pp. 887–889, 2004.

York, D., Evensen, N., Martínez, M., and Delgado, J.: Unified equations for the slope, intercept, and stan-

dard errors of the best straight line, American Journal of Physics, 72, 367–375, http://dx.doi.org/10.1119/1.1632486doi:10.1119/1.1632486, 2004.

Table 1. Filters applied to the ACOS v2.8 data. The filters that differ from the master quality flag are the χ^2 filter cut-off values, the surface pressure filter and the aerosol optical depth filter. (The quantity f_{year} is the fractional year (i.e., 2009.4). The first GOSAT measurements were recorded on 2009.26.) The additional filters that are not included in the master quality flag are listed below the line. The aerosol optical depth is measured at 0.755 µm.

Filter	Filter criterion
Retain data with good spectral fits	reduced_chi_squared_o2_fph $< 1.2 + 0.088 \times (f_{\mathrm{year}} - 2009.26)$
	reduced_chi_squared_strong_co2_fph $< 1.2 + 0.040 \times (f_{\mathrm{year}} - 2009.26)$
	reduced_chi_squared_weak_co2_fph $< 1.2 + 0.064 \times (f_{\mathrm{year}} - 2009.26)$
Retain data with well-retrieved	$\lvert(\Delta P) - \overline{\Delta P}\rvert < 5$ hPa
surface elevation	$(\Delta P = \mathrm{surface_pressure_fph} - \mathrm{surface_pressure_apriori_fph})$
Retain scenes without extreme aerosol	0.05 $<$ retrieved_aerosol_aod_by_type $<$ 0.15
optical depth values	(use the first of the 5 rows of the matrix)
Retain data with no diverging steps	diverging_steps = 0
Retain scenes with no cloud	cloud_flag = 0
Retain data that converge	outcome_flag = 1 or 2
Retain data with 'H' gain only	gain_flag = 'H '
Retain no glint data	glint_flag = 0
Retain scenes without cloud over ice	$2.4 \times$albedo_o2_fph $-1.13 \times$albedo_strong_co2_fph < 1
Retain scenes unless with nonzero	xco2_uncert $\neq 0$
X_{CO_2} uncertainties	

Table 2. Parameters and values for Eq. (4). The coefficients list the values for three assumptions of the X_{CO_2} field in the Southern Hemisphere: 1, that there is a small seasonal cycle and a 1.89 ppm/year secular increase (i.e., Eq. 4); 2, that there is only a 1.89 ppm yr^{-1} secular increase (i.e., no seasonal cycle); and 3, that there is a small seasonal cycle, a 1.89 ppm yr^{-1} secular increase, and a -1 ppm gradient between 25° S and 55° S. The errors are twice the bootstrapped standard errors. The coefficients have units of ppm/unit of blended albedo, ppm/hPa, ppm/airmass and ppm/(10^7 W cm^{-2} sr^{-1} $(cm^{-1})^{-1}$), respectively.

Parameter	Mean value	Coefficients		
		Assumption 1	Assumption 2	Assumption 3
blended_albedo	0.3	10.5 ± 0.4	10.2 ± 0.4	10.1 ± 0.4
ΔP	10.9 hPa	-0.15 ± 0.01	-0.14 ± 0.01	-0.16 ± 0.01
airmass	2.6	-2.0 ± 0.4	-2.2 ± 0.4	-2.1 ± 0.4
signal_o2	3.4×10^{-7} W cm^{-2} sr^{-1} $(cm^{-1})^{-1}$	-0.25 ± 0.08	-0.23 ± 0.08	-0.24 ± 0.08

Table 3. This table presents the results of three comparisons between northern hemisphere TCCON X_{CO_2} and the ACOS-GOSAT X_{CO_2}. Coincidence between the two datasets are determined either by the T_{700} constraint (ACOS-GOSAT soundings within $\pm$2K, $\pm 10°$ latitude by $\pm 30°$ longitude and 10 days of a TCCON measurement), or a geographic constraint ($\pm 0.5°$ latitude by $\pm 1.5°$ longitude). Biases are computed by subtracting the ACOS-GOSAT X_{CO_2} from the TCCON X_{CO_2}. The 'No Modification' fields include the 0.982 bias correction, but not the correction described by equation 4. The 'Modified' fields have had equation 4 applied. The 'ACOS σ' field lists the mean standard deviation of the ACOS-GOSAT data for a particular location. The column labeled 'N_{med}' is the median number of ACOS-GOSAT spectra involved in a single coincidence for a particular site. The columns labeled 'N_{tot}' are the total numbers of ACOS-GOSAT spectra involved with the comparison for all times at that site. Those values are valid only for the T_{700} coincidence criterion. The averages in parentheses are weighted by N_{tot}. There are no ACOS-GOSAT data coincident with the Eureka site using the geographic constraint.

	T_{700} Coincidence						Geographic Coincidence		
	No Modification		Modified by Equation 4				Modified by Equation 4		
	Bias ppm	ACOS σ ppm	Bias ppm	ACOS σ ppm	N_{med}	N_{tot}	Bias ppm	ACOS σ ppm	N_{tot}
Bialystok	-1.19	3.05	-0.70	2.70	10	700	-0.46	2.68	19
Eureka	-1.57	2.23	-4.71	2.32	12	63	—	—	0
Garmisch	-1.32	2.69	-0.78	2.52	11	765	-6.14	3.57	9
Lamont	0.49	2.25	0.62	1.77	28	2269	0.55	1.83	171
Orleans	-0.39	2.59	-0.12	2.26	9	327	-1.08	2.15	7
ParkFalls	-0.97	3.11	-0.53	2.70	14	791	-1.01	3.08	81
Sodankyla	-3.12	3.98	-2.24	3.78	6	178	0.62	3.44	8
Tsukuba	-1.62	1.56	-1.51	1.50	2	63	-1.50	2.38	57
Average	-1.21 (-0.46)	2.68 (2.63)	-1.25 (-0.18)	2.44 (2.25)	11.5	644.5	-1.13 (-0.40)	2.71 (2.34)	44

Table B1. Filters applied to the ACOS v2.9 data.

Filter	Filter criterion
Retain data with good spectral fits	reduced_chi_squared_o2_fph < 1.4
	reduced_chi_squared_strong_co2_fph < 2
	reduced_chi_squared_weak_co2_fph < 2
Retain data with well-retrieved	$\lvert(\Delta P) - \overline{\Delta P}\rvert < 5$ hPa
surface elevation	$(\Delta P = \text{surface_pressure_fph} - \text{surface_pressure_apriori_fph};\ \overline{\Delta P} = 0.59\ \text{hPa})$
Retain scenes without extreme aerosol	$0.05 <$ retrieved_aerosol_aod_by_type < 0.15
optical depth values	(use the first of the 5 rows of the matrix)
Retain data with 0 or 1 diverging steps	diverging_steps = 0
Retain scenes with no cloud	cloud_flag = 0
Retain data that converge	outcome_flag = 1 or 2
Retain data with 'H' gain only	gain_flag = 'H '
Retain scenes without cloud over ice	$2.4 \times$albedo_o2_fph $-1.13 \times$albedo_strong_co2_fph < 1
Glint data are defined by	sounding_land_fraction = 0
	$\lvert$sounding_solar_zenith $-$ sounding_zenith$\rvert < 2°$
	$160° <$ sounding_solar_azimuth $-$ sounding_azimuth $< 200°$

Table B2. This table presents the results of three comparisons between northern hemisphere TCCON X_{CO_2} and the ACOS-GOSAT X_{CO_2} for the v2.9 ACOS-GOSAT data. Coincidence between the two datasets are determined either by the T_{700} constraint (ACOS-GOSAT soundings within $\pm$2K, $\pm 10°$ latitude by $\pm 30°$ longitude and 10 days of a TCCON measurement), or a geographic constraint ($\pm 0.5°$ latitude by $\pm 1.5°$ longitude). Biases are computed by subtracting the ACOS-GOSAT X_{CO_2} from the TCCON X_{CO_2}. The 'No Modification' fields have not had the v2.9 correction applied. The 'Modified' fields have had the v2.9 correction applied. The 'ACOS σ' field lists the mean standard deviation of the ACOS-GOSAT data for a particular location. The column labeled 'N_{med}' is the median number of ACOS-GOSAT spectra involved in a single coincidence for a particular site. The columns labeled 'N_{tot}' are the total numbers of ACOS-GOSAT spectra involved with the comparison for all times at that site. Those values are valid only for the T_{700} coincidence criterion. The averages in parentheses are weighted by N_{tot}. There are no ACOS-GOSAT data coincident with the Eureka site using the geographic constraint.

	T_{700} Coincidence						Geographic Coincidence		
	No Modification		Modified				Modified		
	Bias ppm	ACOS σ ppm	Bias ppm	ACOS σ ppm	N_{med}	N_{tot}	Bias ppm	ACOS σ ppm	N_{tot}
Bialystok	-0.08	3.08	0.49	2.90	12	869	1.67	3.93	27
Eureka	-0.97	3.35	-1.88	3.41	10	60	—	—	0
Garmisch	-0.06	2.50	0.40	2.44	15	1004	-3.44	4.23	16
Lamont	0.81	1.97	0.98	1.88	38	2668	0.86	1.92	251
Orleans	-0.41	2.18	0.21	1.95	14	430	-0.18	2.19	13
ParkFalls	-0.15	3.00	0.36	2.69	18	1018	0.03	3.21	120
Sodankyla	-2.35	3.19	-1.58	3.17	7	254	-0.34	4.23	16
Tsukuba	-0.72	1.70	-0.57	1.70	3	46	-1.03	2.65	59
Average	-0.49 (0.16)	2.62 (2.45)	-0.20 (0.53)	2.52 (2.31)	14.63	793.6	-0.30 (0.28)	2.79 (2.58)	62.8

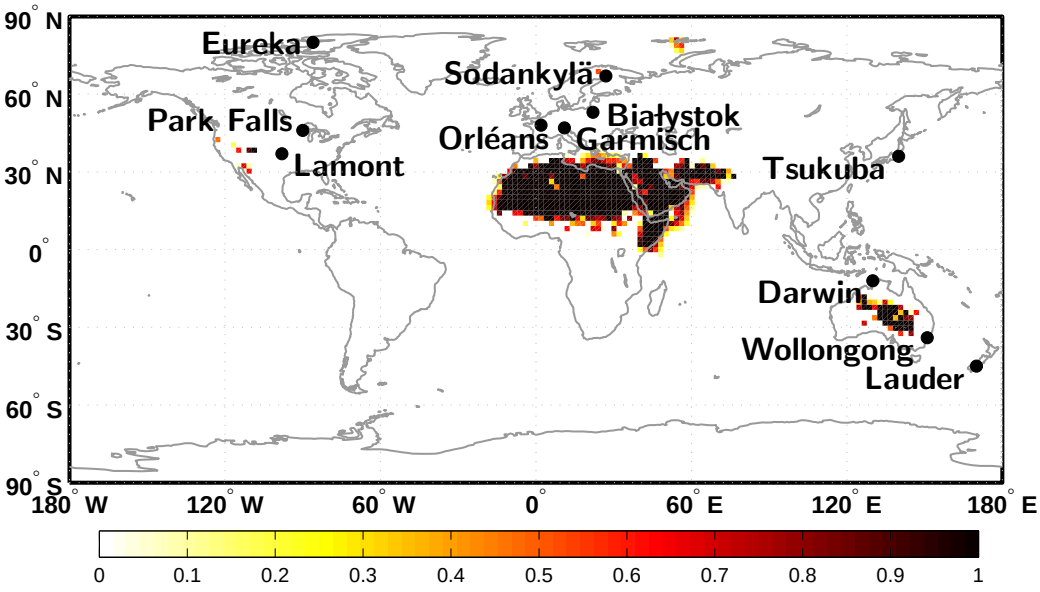

Fig. 1. The locations of the TCCON stations used in this study are shown in black circles. The fraction of soundings in a 2° by 2° box that are M-gain (and removed) are shown in the colours.

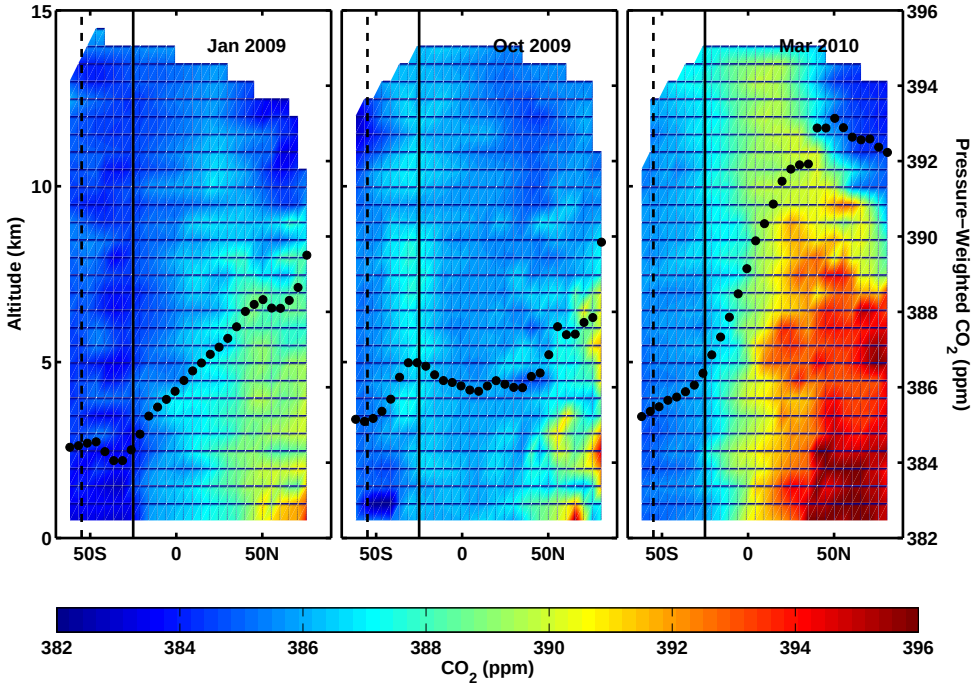

Fig. 2. Three slices of the atmospheric CO_2 are plotted for the three HIPPO flights at different times of the year. Most of these data were measured over the Pacific Ocean. There is generally smaller variability in the Southern Hemisphere south of 25° S (indicated by the solid vertical black line) than in the Northern Hemisphere. 99.9 % of the filtered ACOS-GOSAT data in the Southern Hemisphere south of 25° S lie between 25° S and 55° S (indicated by the dashed vertical black line). The black circles are the pressure-weighted mean mixing ratios at each 5-degree latitude bin, with their values on the right axis. Note that the black circles are not total column amounts, and will be affected by missing data in the stratosphere.

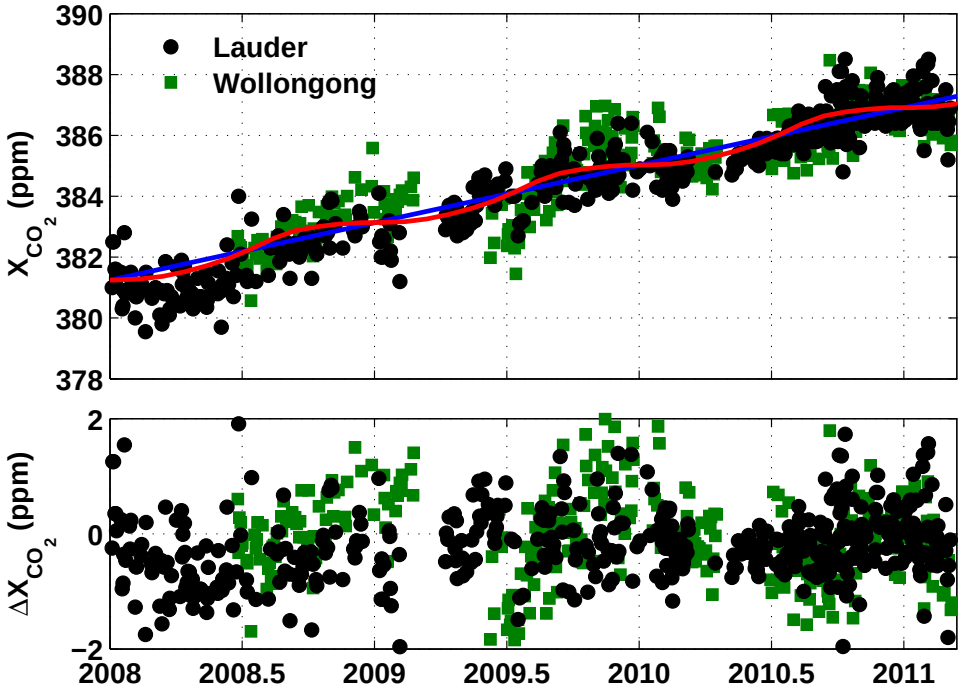

Fig. 3. The time series of the Southern Hemisphere TCCON data from Lauder, New Zealand and Wollongong, Australia are plotted in the top panel, along with the 1.89 ppm yr^{-1} secular increase (blue). The Baring Head GLOBALVIEW climatological seasonal cycle with a time lag of 6 weeks and a reduced amplitude ($\times 0.65$) is superimposed on the secular increase (red). In the bottom panel, the red curve is removed from the Lauder and Wollongong data to show the residuals.

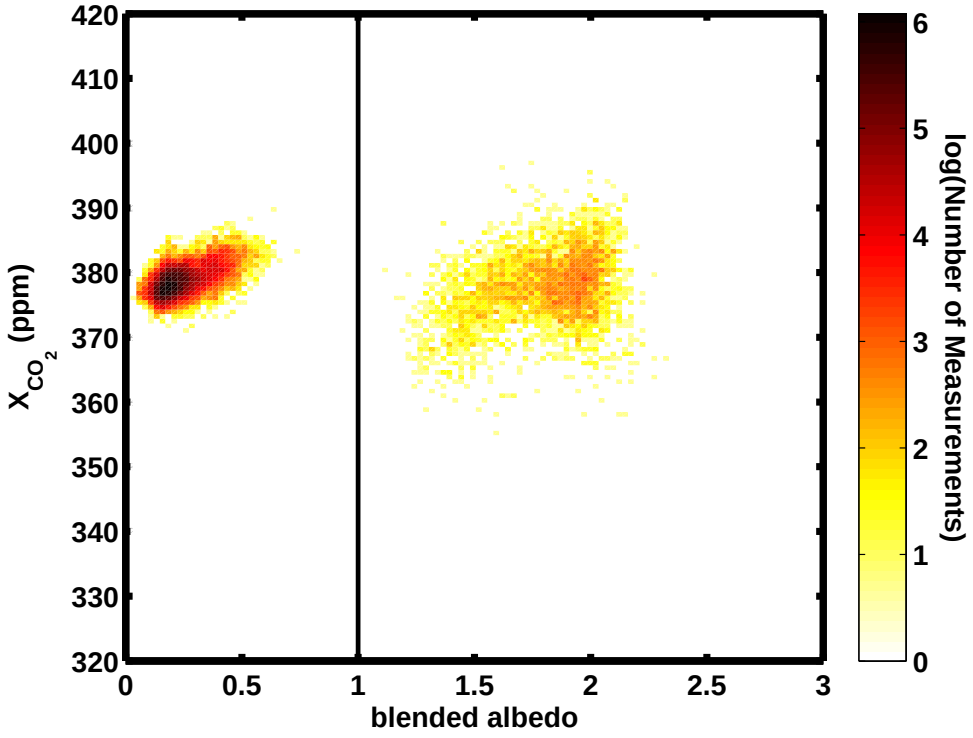

Fig. 4. An illustration of how snowy or icy scenes affect the ACOS-GOSAT data. There are two clear populations of points, delineated by a value of 1 in blended albedo (defined in Eq. 2 of the main text). Points to the left of the line at 1 are not influenced by snow and ice, and they are retained; points to the right are discarded. The colours represent the logarithm of the number of measurements in each 0.7 ppm by 0.025 units of blended albedo. The data in this figure are from soundings poleward of 25°S and span April 6, 2009 through March 21, 2011.

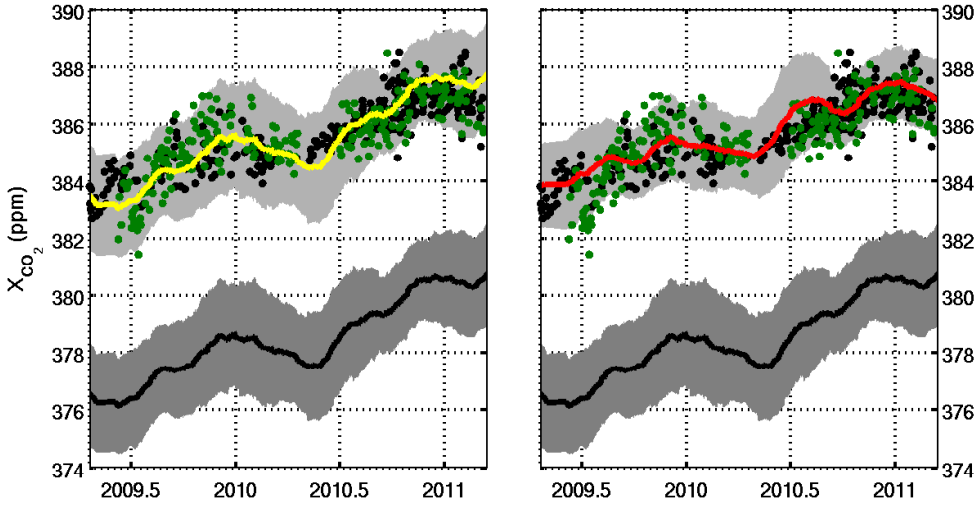

Fig. 5. The black curve is the original, unmodified ACOS-GOSAT data between 25° S and 55° S in both panels. The global bias (0.982) between the ACOS-GOSAT and TCCON data is removed in the left panel to obtain the yellow curve, and Eq. (4) is applied to obtain the red curve in the right panel. The grey shading represents 1σ. The TCCON data from Lauder, New Zealand (black circles) and Wollongong, Australia (green circles) are plotted for comparison.

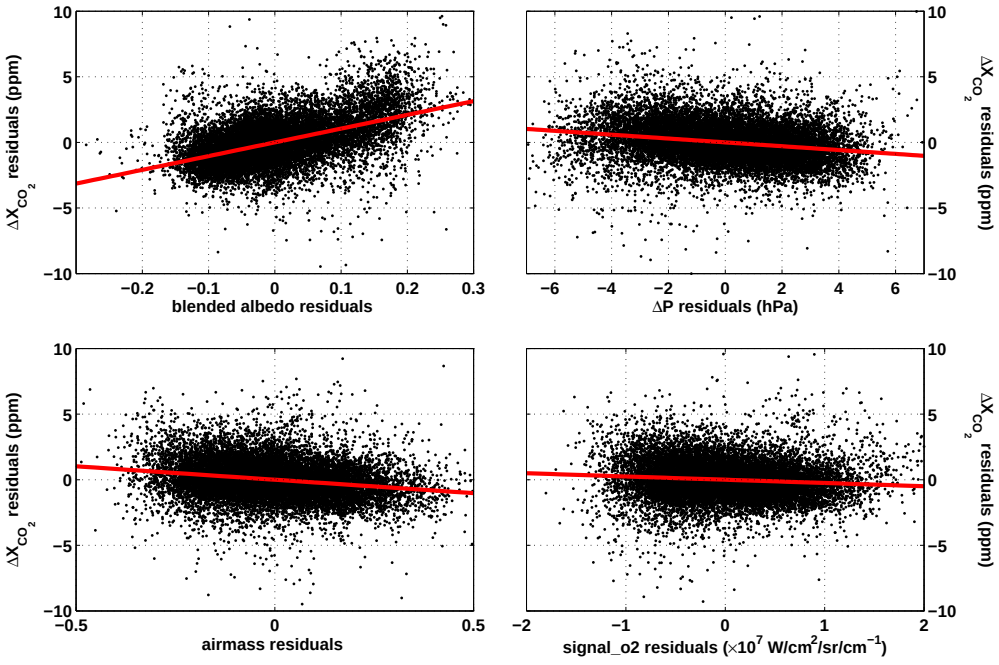

Fig. 6. Scatter plots showing the individual relationships between ΔX_{CO_2} and the covariates simultaneously fitted in Eq. (4). These are data only from the Southern Hemisphere, where there should be no significant X_{CO_2} variations. The solid red lines are the best fit lines described by the coefficients listed in Table 2.

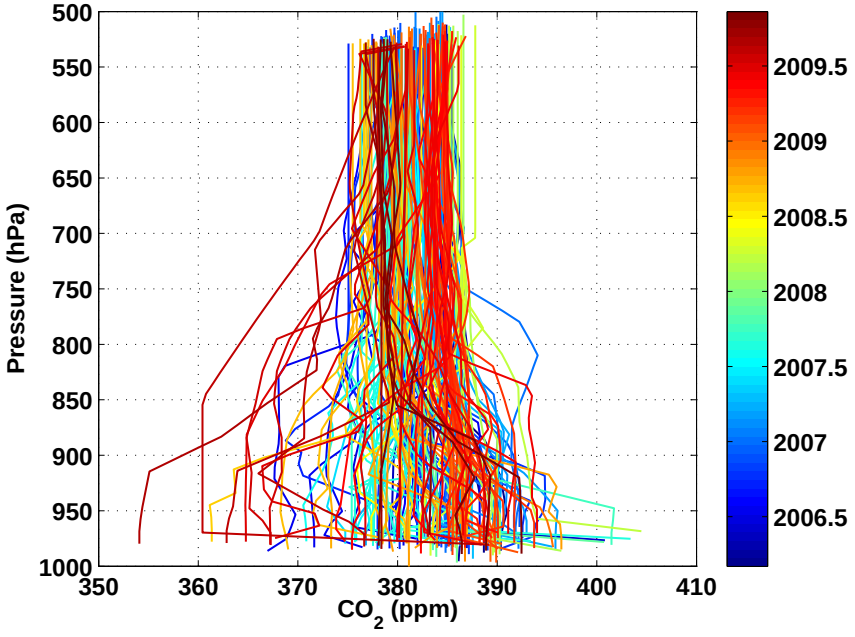

Fig. 7. All the Cessna profiles over Lamont, OK, are shown on a pressure grid, coloured by the time the profile was measured. These profiles are detrended to show only the seasonality and variability.

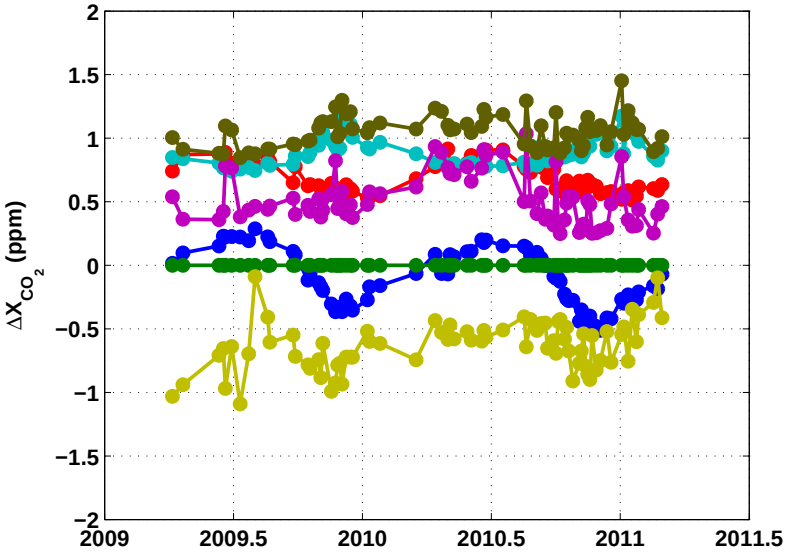

Fig. 8. The curves in this figure show the effect of the choice of a priori profile, and the effect of smoothing by the averaging kernels for data measured over the Lamont TCCON site. Plots show the ACOS-GOSAT adjustment to the ensemble profile ($\sum_j h_j (\boldsymbol{a}_1 - \boldsymbol{u})_j^T (\boldsymbol{x}_{\mathrm{a1}} - \boldsymbol{x}_{\mathrm{c}})_j$, blue), the TCCON adjustment to the ensemble profile ($\sum_j h_j (\boldsymbol{a}_2 - \boldsymbol{u})_j^T (\boldsymbol{x}_{\mathrm{a2}} - \boldsymbol{x}_{\mathrm{c}})_j = 0$, green), the smoothing error ($\sqrt{\sum_k \sum_j h_j (\boldsymbol{a}_1 - \boldsymbol{a}_2)_j^T (\mathbf{S}_{\mathrm{c}})_{jk} (\boldsymbol{a}_1 - \boldsymbol{a}_2)_k}$, red), the ACOS-GOSAT standard deviation (σ_1, cyan), the TCCON standard deviation (σ_2, purple), the difference between the TCCON adjusted ACOS-GOSAT smoothed values ($\hat{c}'_{12} - \hat{c}'_2$, yellow) and the square root of the sum of the TCCON and ACOS-GOSAT variances ($\sqrt{\sigma_1^2 + \sigma_2^2}$, dark green). All parameters are defined in Appendix A.

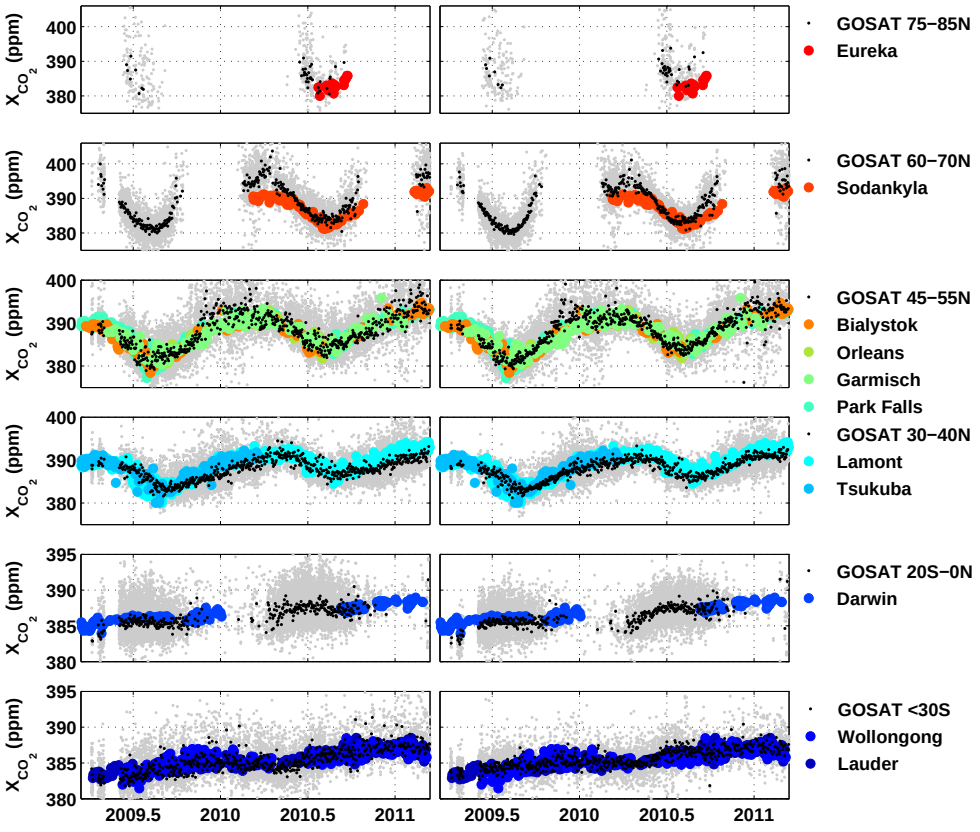

Fig. 9. Seasonal-cycle comparisons. These panels show the ACOS-GOSAT data adjusted by only the global bias (0.982, left panels) and after applying Eq. (4) (right panels). Each row of panels shows a different latitude range for the ACOS-GOSAT data (the black dots are the daily median zonal average values, and the grey dots are the individual measurements), and the TCCON daily median data within the latitude band (multi-coloured circles). The agreement and variability in the ACOS-GOSAT data are visibly improved in the right-hand panels.

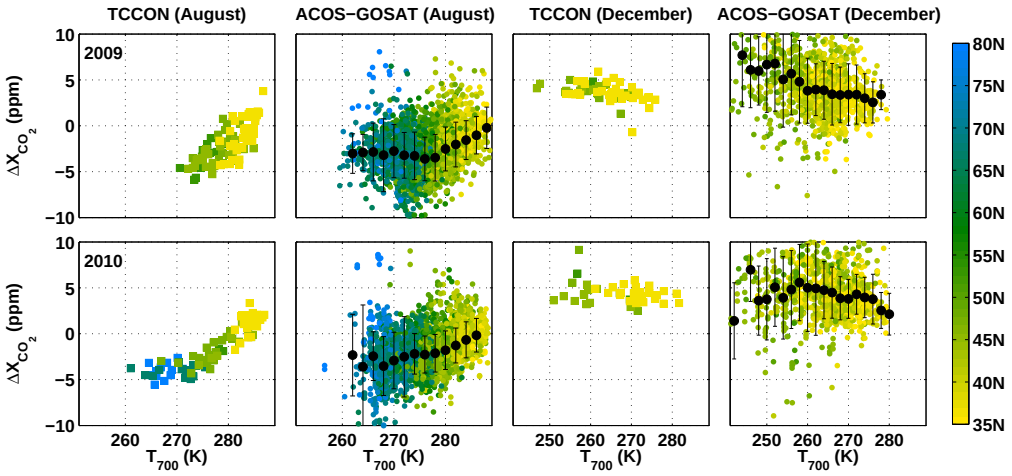

Fig. 10. Plotted here are X_{CO_2} anomalies against the temperature at 700 hPa. The anomalies are computed by subtracting a 1.89 ppm yr^{-1} secular increase from the X_{CO_2} time series. There is a strong positive relationship in the summertime, and this relationship reverses in sign in the winter. The top row of panels shows data from 2009, and the bottom row shows data from 2010. The first two columns of panels contain data from August, and the right two columns show December. The TCCON data are plotted in squares; the modified ACOS-GOSAT data are circles, and the medians and standard deviations of the ACOS-GOSAT data at each 2 K bin are plotted in black circles with error bars. The colours represent the latitude. Although there are no TCCON data at the highest latitudes (lowest T_{700}) in 2009, the TCCON sites operating in both years show visibly different drawdown characteristics (indicated by the larger variability in ΔX_{CO_2} near 280K) in the August 2009 than in the 2010 TCCON data. This is indistinguishable within the standard deviation of the ACOS-GOSAT data. The ACOS-GOSAT data nicely capture the reversal in sign of the X_{CO_2}-T_{700} slope in the winter.

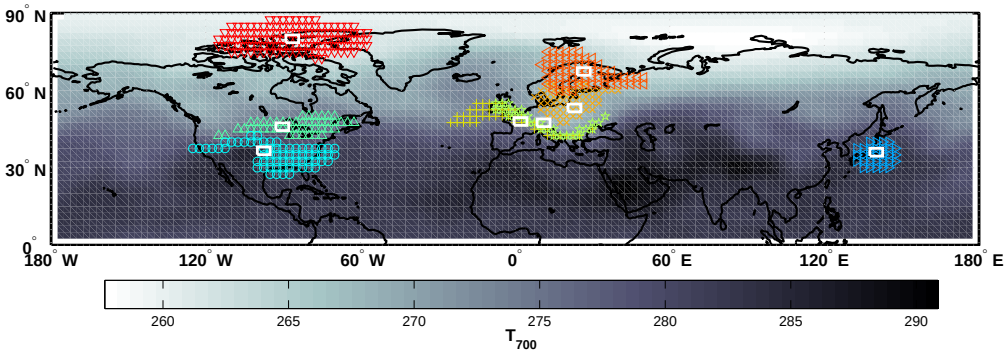

Fig. 11. A map of the areas that fulfill the coincidence criteria for a ten-day period in August, 2010. The background T_{700} field is from the NCEP/NCAR analysis. The white boxes show the $\pm 0.5°$ latitude and $\pm 1.5°$ longitude limits about each TCCON site. The symbols in colour show the locations on the Earth for this ten-day period that satisfy the coincidence criteria that T_{700} is within ± 2 K, latitude is within $\pm 10°$, and longitude is within $\pm 30°$. (The only exception to this is the Tsukuba site, where the longitude criterion is tightened to $\pm 10°$ to avoid over-weighting data over China.) The actual locations of the coincidences with the ACOS-GOSAT data are restricted to the regions overlaid in colour, where the ACOS-GOSAT data exist (i.e., only over land and in cloud-free scenes).

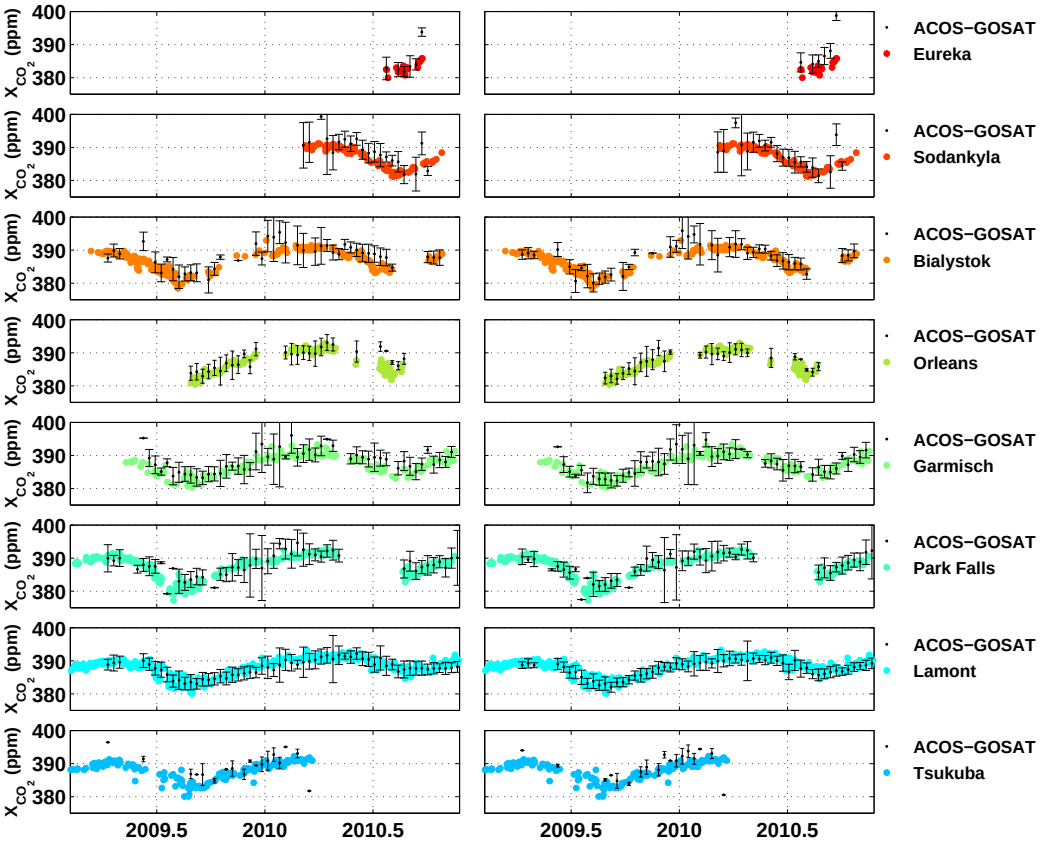

Fig. 12. A site-by-site comparison between ACOS-GOSAT and the Northern Hemisphere TCCON sites, using the T_{700} coincidence criterion (data recorded within 10 days, $\pm 10°$ latitude, $\pm 30°$ longitude and ± 2K). The left panel shows the ACOS-GOSAT data after applying the global bias (0.982), and the right panel shows the data after applying Eq. (4).

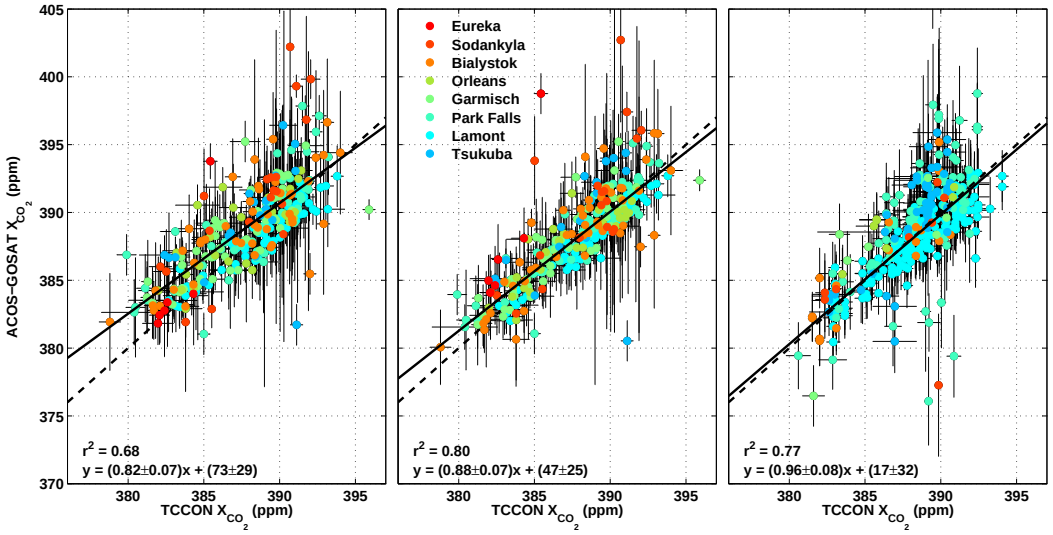

Fig. 13. The left two panels show the regression between TCCON and ACOS-GOSAT using the T_{700} coincidence criterion (10 days, $\pm 10°$ latitude, $\pm 30°$ longitude and ± 2K). The left panel shows the large-scale bias-corrected, but otherwise unmodified, data. The middle panel shows the regression after applying Eq. (4). The right-hand panel shows the regression after applying Eq. (4), but using coincidence criteria that restricts latitudes to within $\pm 0.5°$, longitudes to within $\pm 1.5°$, and interpolates the TCCON data onto the ACOS-GOSAT measurement times. Note that there are no coincident data over Eureka when using the geographic coincidence criteria (right-hand panel). The solid lines show the best fit to the data (with equations and ± 2 standard errors shown on the plot), and the one-to-one line is plotted as a dashed line. The vertical bars represent the $\pm 2\sigma$ variability of the ACOS-GOSAT data, illustrating the dependence of the variability of the ACOS-GOSAT data at each TCCON value (i.e., var(y|x)) in the regression. Similarly, the horizontal bars represent the $\pm 2\sigma$ variability of the TCCON data.

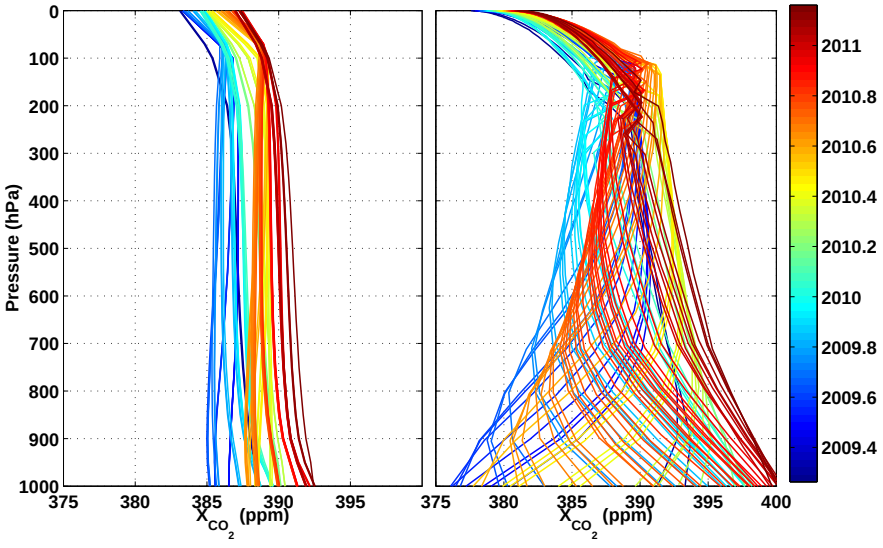

Fig. A1. A priori profiles at the Lamont TCCON site for ACOS-GOSAT (left panel) and TCCON (right panel), coloured by the year.

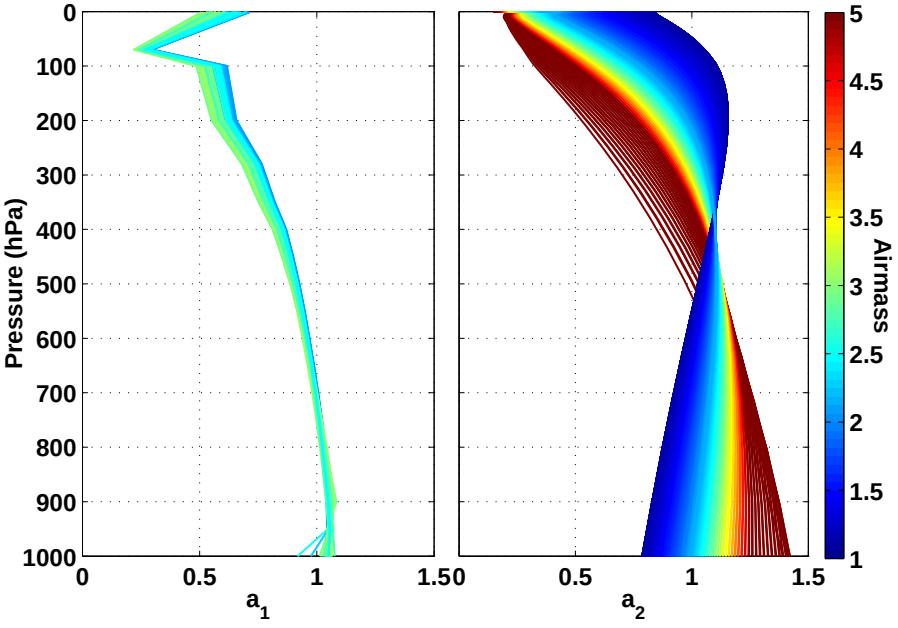

Fig. A2. Column averaging kernels for ACOS-GOSAT (left panel) and TCCON (right panel), coloured by the airmass. The GOSAT airmass range plotted here is much smaller than the range of TCCON airmasses.

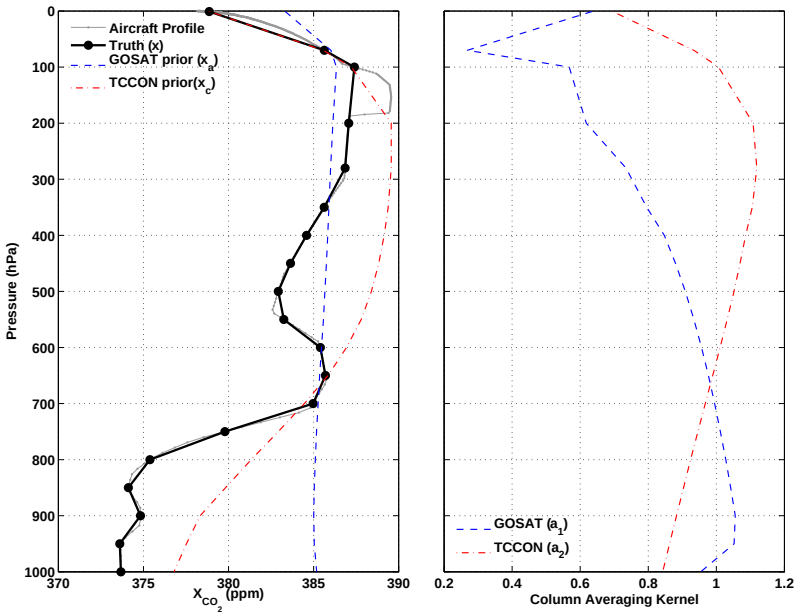

Fig. A3. Plots from 2 August 2009, when there was an overflight of Lamont that spanned a large altitude range (0–12 km). The left panel shows the aircraft profile (grey) which uses the TCCON a priori profile to fill in the stratosphere above the aircraft ceiling, the true profile (black; i.e., the aircraft profile interpolated onto the ACOS retrieval grid), the ACOS-GOSAT a priori profile (blue) and the TCCON a priori profile (red). The right panel shows the ACOS-GOSAT (blue) and TCCON (red) column averaging kernels for the time of the aircraft measurement.

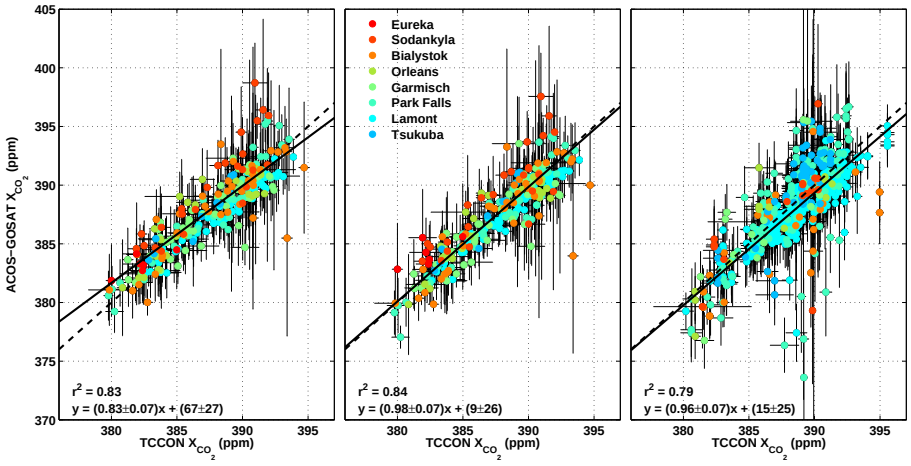

Fig. B1. The left two panels show the regression between TCCON and ACOS-GOSAT v2.9 data using the T_{700} coincidence criterion. The left panel shows the unmodified data. The middle panel shows the regression after applying Eq. (4) but with the coefficients described in Appendix B. The right-hand panel shows the regression after applying Eq. (4) with the coefficients described in Appendix B, but using coincidence criteria that restricts latitudes to within $\pm 0.5^\circ$, longitudes to within $\pm 1.5^\circ$, and interpolates the TCCON data onto the ACOS-GOSAT measurement times. Note that there are no coincident data over Eureka when using the geographic coincidence criteria (right-hand panel). The solid lines show the best fit to the data (with equations and ± 2 standard errors shown on the plot), and the one-to-one line is plotted as a dashed line. The vertical bars represent the $\pm 2\sigma$ variability of the ACOS-GOSAT data, illustrating the dependence of the variability of the ACOS-GOSAT data at each TCCON value (i.e., var(y|x)) in the regression. Similarly, the horizontal bars represent the $\pm 2\sigma$ variability of the TCCON data.

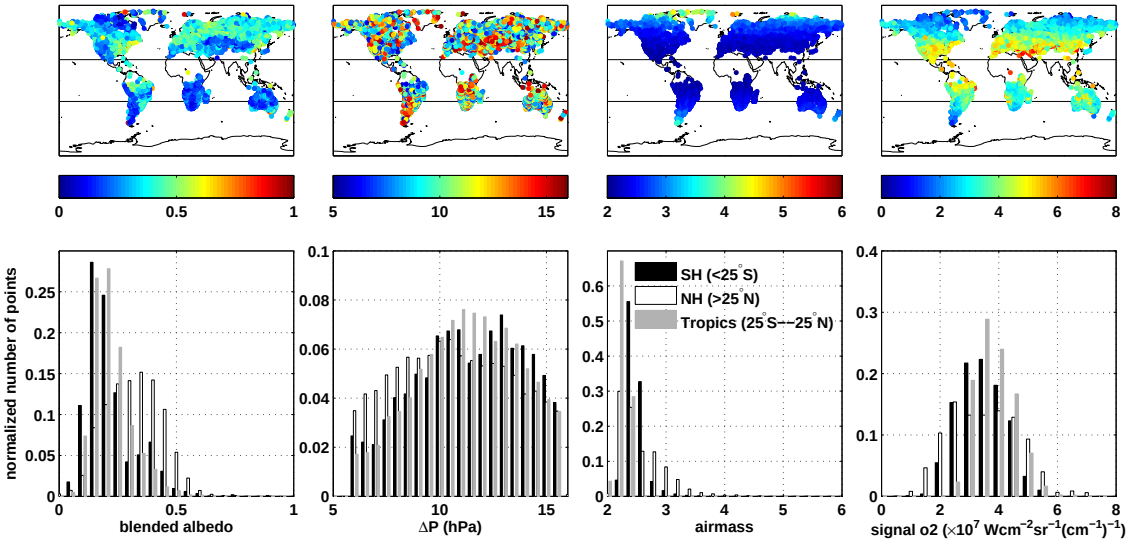

Fig. S1. A map and histogram of the parameters used in equation 4 in August.

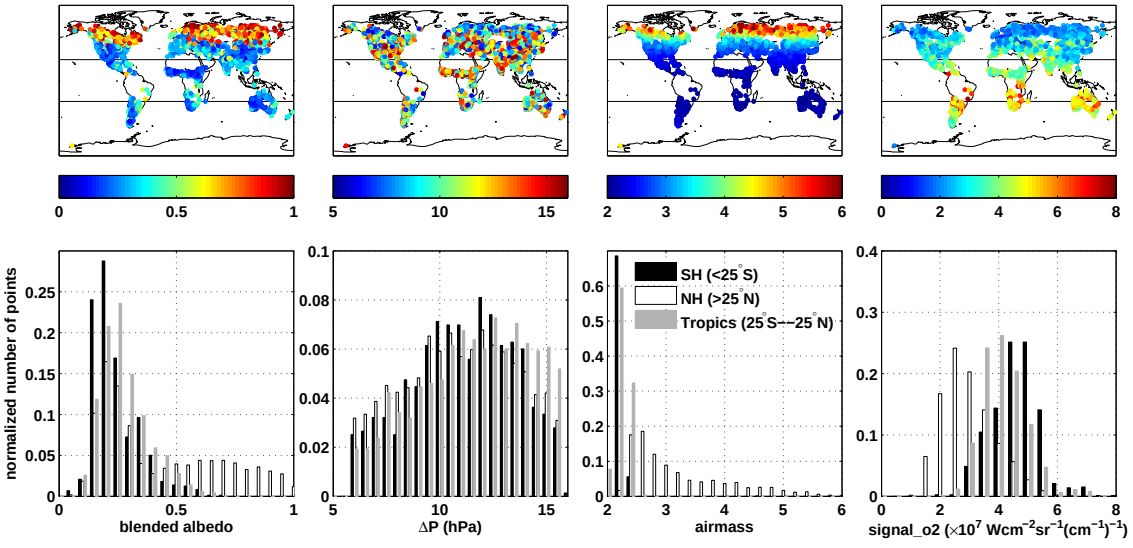

Fig. S2. A map and histogram of the parameters used in equation 4 in February.

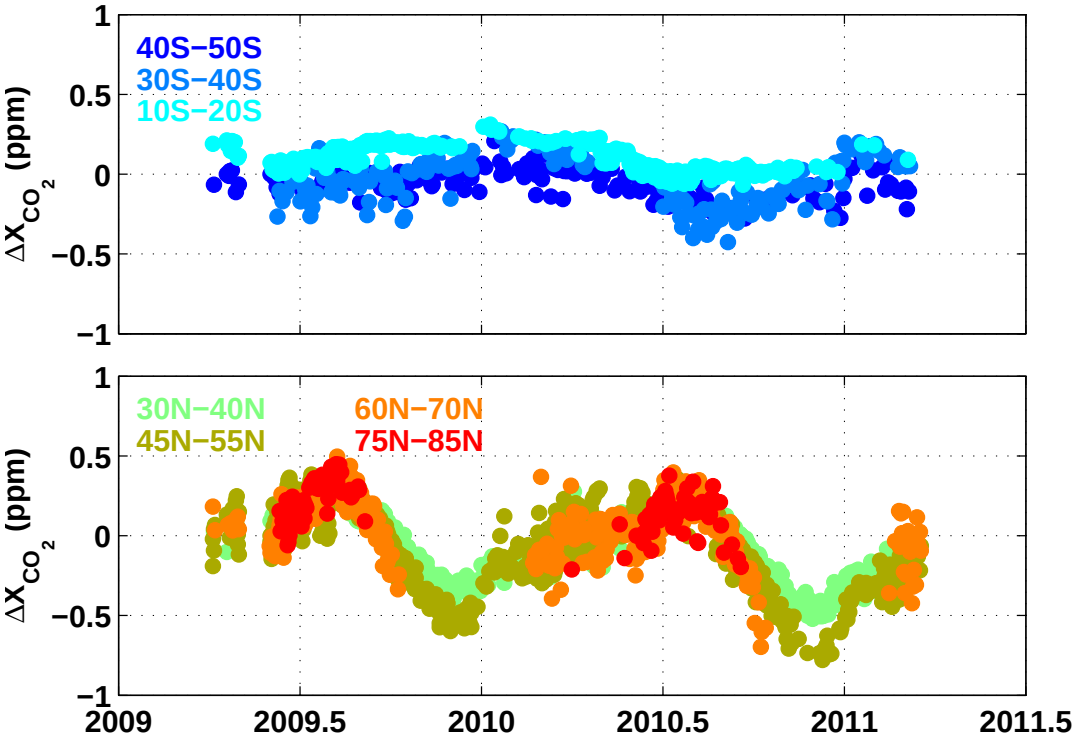

Fig. S3. The latitude-dependence of the difference between using the TCCON *a priori* profile and the ACOS *a priori* profile (TCCON−ACOS plotted here) on the ACOS-GOSAT retrievals (e.g., $\hat{c}_1' - \hat{c}_1$ from equation A10). The latitudes are binned around TCCON sites.

DISCLAIMER

This document was prepared as an account of work sponsored by the United States Government. While this document is believed to contain correct information, neither the United States Government nor any agency thereof, nor The Regents of the University of California, nor any of their employees, makes any warranty, express or implied, or assumes any legal responsibility for the accuracy, completeness, or usefulness of any information, apparatus, product, or process disclosed, or represents that its use would not infringe privately owned rights. Reference herein to any specific commercial product, process, or service by its trade name, trademark, manufacturer, or otherwise, does not necessarily constitute or imply its endorsement, recommendation, or favoring by the United States Government or any agency thereof, or The Regents of the University of California. The views and opinions of authors expressed herein do not necessarily state or reflect those of the United States Government or any agency thereof or The Regents of the University of California.

Ernest Orlando Lawrence Berkeley National Laboratory is an equal opportunity employer.